Tsunami Simulation and Detection Using Global Navigation Satellite System Reflectometry

by

© Qingyun Yan, B.Eng.

A thesis submitted to the School of Graduate Studies

in partial fulfilment of the requirements for the degree of

Master of Engineering

Department of Electrical and Computer Engineering

Faculty of Engineering and Applied Science

Memorial University of Newfoundland

May, 2016

St. John's   Newfoundland

Abstract

In this thesis, research for tsunami remote sensing using the Global Navigation Satellite System-Reflectometry (GNSS-R) delay-Doppler maps (DDMs) is presented.

Firstly, a process for simulating GNSS-R DDMs of a tsunami-dominated sea surface is described. In this method, the bistatic scattering Zavorotny-Voronovich (Z-V) model, the sea surface mean square slope model of Cox and Munk, and the tsunami-induced wind perturbation model are employed. The feasibility of the Cox and Munk model under a tsunami scenario is examined by comparing the Cox and Munk model-based scattering coefficient with the Jason-1 measurement. A good consistency between these two results is obtained with a correlation coefficient of 0.93. After confirming the applicability of the Cox and Munk model for a tsunami-dominated sea, this work provides the simulations of the scattering coefficient distribution and the corresponding DDMs of a fixed region of interest before and during the tsunami. Furthermore, by subtracting the simulation results that are free of tsunami from those with presence of tsunami, the tsunami-induced variations in scattering coefficients and DDMs can be clearly observed.

Secondly, a scheme to detect tsunamis and estimate tsunami parameters from such tsunami-dominant sea surface DDMs is developed. As a first step, a procedure to determine tsunami-induced sea surface height anomalies (SSHAs) from DDMs is demonstrated and a tsunami detection precept is proposed. Subsequently, the tsunami parameters (wave amplitude, direction and speed of propagation, wavelength, and the tsunami source location) are estimated based upon the detected tsunami-induced SSHAs. In application, the sea surface scattering coefficients are unambiguously retrieved by employing the spatial integration approach (SIA) and the dual-antenna technique. Next, the effective wind speed distribution can be restored from the scattering coefficients. Assuming all DDMs are of a tsunami-dominated sea surface, the tsunami-induced SSHAs can be derived with the knowledge of background wind speed distribution. In addition, the SSHA distribution resulting from the tsunami-free DDM (which is supposed to be zero) is considered as an error map introduced during the overall retrieving stage and is utilized to mitigate such errors from influencing subsequent SSHA results. In particular, a tsunami detection procedure is conducted to judge the SSHAs to be truly tsunami-induced or not through a fitting process, which makes it possible to decrease the false alarm. After this step, tsunami parameter estimation is proceeded based upon the fitted results in the former tsunami detection procedure. Moreover, an additional method is proposed for estimating tsunami propagation velocity and is believed to be more desirable in real-world scenarios.

The above-mentioned tsunami-dominated sea surface DDM simulation, tsunami detection precept and parameter estimation have been tested with simulated data based on the 2004 Sumatra-Andaman tsunami event.

Acknowledgements

Contents

List of Tables

List of Figures

Table of Acronyms

The page numbers here indicate the place of first significant reference.

PDF :   Probability density function (p. 15).

WS :   Wind speed (p. 16).

MSS :   Mean square slope (p. 16).

2-D :   Two-dimensional (p. 38).

RMSE :   Root mean square error (p. 45).

CYGNSS :   Cyclone Global Navigation Satellite System (p. 65).

Table of Symbols

The page numbers here indicate the place of first significant reference. Although not all symbols are explicitly referenced below, their definitions are obvious from the context.

$\langle |Y(\Delta\tau, \Delta f)|^2 \rangle :$ Power of received signal (p. 11).

$\vec{\rho} :$ The position vector of observed surface point with respect to Specular Point (SP) (p. 11).

$\Delta\tau = \tau(\vec{\rho}) - \tau :$ τ and $\tau(\vec{\rho})$ are the delays at SP and the observed surface point, respectively (p. 11).

$\Delta f = f_d(\vec{\rho}) - f_d :$ f_d and $f_d(\vec{\rho})$ are the Doppler shifts at SP and the observed surface point, respectively (p. 11).

$T_i :$ The coherent integration time (p. 11).

$D :$ Antenna radiation pattern (p. 11).

$R_T :$ The distance from the transmitter to a point on the oceans surface (p. 11).

$R_R :$ The distance from the receiver to a point on the oceans surface (p. 11).

σ^0 : Dimensionless scattering coefficient (p. 11).

A : Scattering surface, approximately the Glistening Zone (GZ) (p. 11).

$\Lambda(\Delta\tau)$: Triangle pulse function $\Lambda(\Delta\tau) = 1 - |\frac{\Delta\tau}{\tau_c}|$, when $-\tau_c \leq \Delta\tau \leq \tau_c$; $\Lambda(\Delta\tau) = 0$, otherwise (p. 11).

$S(\Delta f)$: Sinc function $S(\Delta f) = \sin(\pi T_i \Delta f)/(\pi T_i \Delta f)$ (p. 11).

τ_c : $\tau_c = 1/1023$ ms is the length of a chip of the coarse/acquisition (C/A) code (p. 12).

$|\Re|^2$: The Fresnel reflection coefficient (p. 15).

$P(\cdot)$: Probability density function (p. 15).

$\vec{q}$: Scattering vector (p. 15).

$\vec{s}$: Ocean surface slope (p. 15).

ϕ_0 : The angle between the wind direction and the x-axis (p. 15).

σ_u^2 : Upwind sea surface slope variance (p. 15).

σ_c^2 : Crosswind sea surface slope variance (p. 15).

U_{10} : Wind speed (WS) at 10 m height above sea level (p. 16).

WS_{eff} : The effective wind speed during a tsunami (p. 17).

WS_0 : The background wind speed before a tsunami (p. 17).

M : A factor to distinguish WS_{eff} from WS_0 (p. 17).

κ : $\kappa = 0.4$ is the von Karman constant (p. 17).

u_* : The friction velocity (p. 17).

H : The height of the background logarithmic boundary layer (p. 17).

a : The tsunami-induced sea surface height change (p. 17).

c : The tsunami propagation velocity (p. 17).

D : The depth of sea (p. 17).

g : The acceleration due to gravity (p. 17).

z_0 : The roughness length (p. 17).

T_0 : The tsunami period (p. 17).

A : Amplitude of fitted SSHA profile (p. 44).

k : Non-directional wave number of fitted SSHA profile (p. 44).

ϕ : Phase shift of fitted SSHA profile (p. 44).

r : The range variable associated with fitted SSHA profile (p. 44).

λ : Tsunami wavelength of fitted SSHA profile (p. 45).

$\Delta\phi$: Phase shift difference between each fitted SSHA profile (p. 47).

$\Delta\phi_{mn}$: Phase shift difference between mth and nth fitted SSHA profiles (p. 47).

Δt_{mn} : Time difference between mth and nth fitted SSHA profiles (p. 47).

Chapter 1

Introduction

In this chapter, the importance of tsunami remote sensing and the significance of Global Navigation Satellite System Reflectometry (GNSS-R) signals for tsunami detection are demonstrated first. Then, the literature about GNSS-R applications in remote sensing, particularly tsunami detection is summarized. Last, the scope of this thesis is outlined.

1.1   Research Rationale

Tsunamis are long-period gravity waves generated by impulsive vertical displacements of water column. Such sudden displacements are usually caused by submarine earthquakes, volcanic eruptions, landslides, human-made explosions, and the collision of bolides into the ocean [1]. In addition, tsunami wave manifests its characteristics in terms of high propagation speed in the deep sea (up to 1000 km/h) and considerable high wave height nearshore (may reach heights of 30 m or more).

It has been widely recognized that tsunamis are one of the devastating natural hazards for coastal communities. Coastal areas are extremely vulnerable to tsunami hazards due to a growing population (already over one-third of the world's population) and rapid developments [2]. For example, the Sumatra-Andaman tsunami that occurred in 2004 claimed about 250,000 human lives and caused tremendous damage to neighbouring countries [2]. Therefore, tsunami detection is especially important.

Establishments of numerous tsunami warning centers, e.g., the U.S. Pacific Tsunami Warning Center [3] have made it possible to reduce the threat of tsunamis. Typically, data collected from a network of seismic stations are utilized by warning centers to detect tsunamis. When tsunami waves propagate over the station, bottom pressure fluctuations that are proportional to the tsunami-induced sea surface elevations will be recorded and such information will be reported to a surface buoy, which is integrated with a micro-computer with telecommunications capability, via an acoustic link, see Figure 1.1 (this figure is the work of National Data Buoy Center/NOAA, at http://www.ndbc.noaa.gov/dart/dart.shtml). In addition, another system, the German Indonesian Tsunami Early Warning System consists of hundreds of sensor systems including the Global Navigation Satellite System (GNSS) receivers, and it is able to determinate sea levels and to detect co-seismic land mass displacements [4]. In general, these systems deduce the tsunami information based on the empirical/modelled relationship between tsunami source (e.g., earthquake) parameters and tsunami wave parameters [5].

The conventional buoy measurement is originally designed to obtain ocean wave statistics [5]. Tsunami waves may be detected when they travel over the sea surface where buoy monitoring is available. However, the number of buoys placed around the
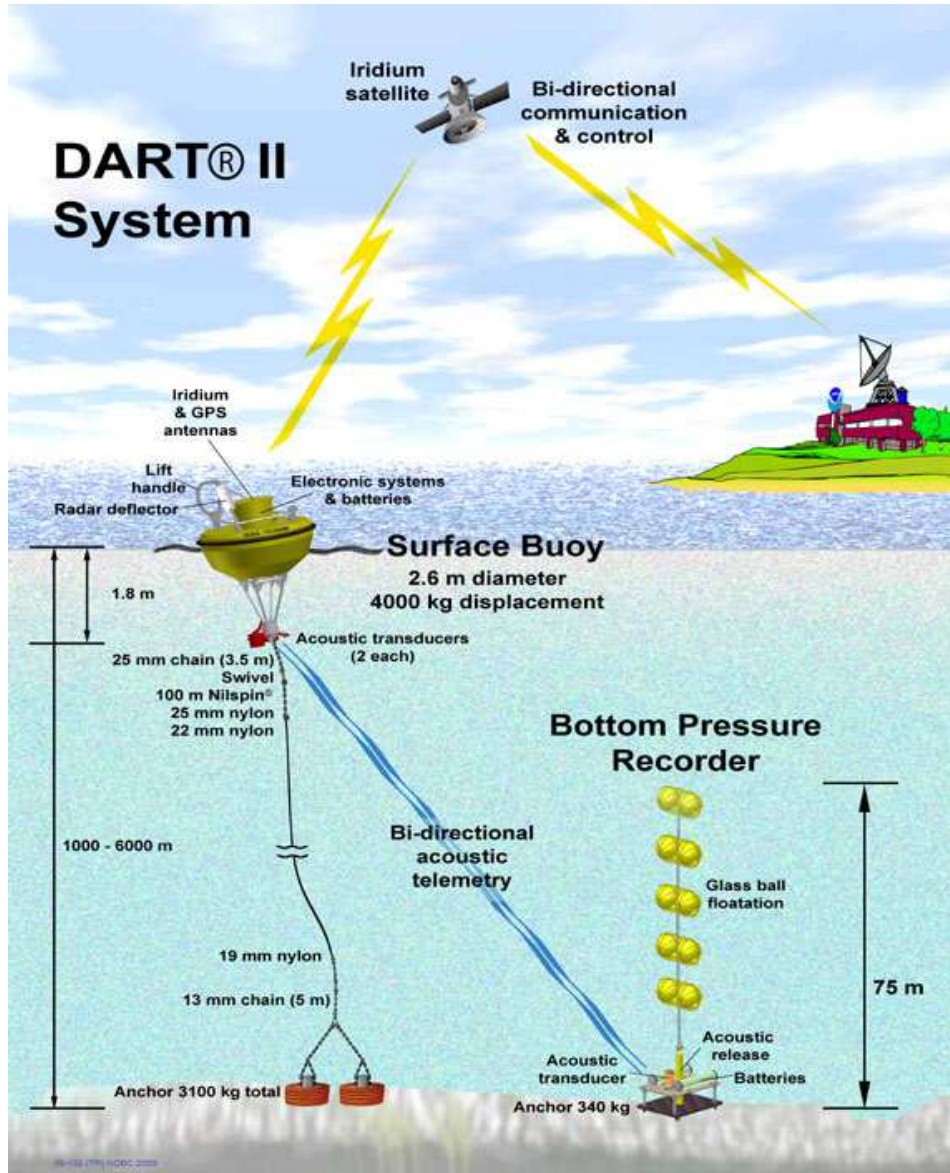
Figure 1.1: Deep-Ocean Assessment and Reporting of Tsunami System.

world is limited and the measurement coverage of a buoy is confined, which means only an extremely restricted area of the sea can be measured. In addition, costs of buoy deployment, operation and maintenance are very high. Moreover, a sufficient observation period of tsunami based on buoys can last up to several hours [5], during which tsunami waves may have already arrived at the shore. Thus, buoy measurement is a costly and inefficient method to detect tsunamis.

The satellite altimeter may provide some direct information about the tsunami, such as sea surface height (SSH) and the radar backscattering coefficient. For example, Jason-1 satellite altimeter encountered the 2004 Sumatra-Andaman tsunami on its path 109 for cycle 129, thereby offering valuable data on tsunami measurement [6]. However, the fact is only a handful definitive SSH changes due to a tsunami event have been measured out of more than 150 documented tsunami events since the launch of the TOPEX/Poseidon satellite altimeter in 1992 [7]. This is mainly because of the constrained areas covered by the satellite altimeter along-track measurement [6].

High-frequency (HF) radar is also believed to possess the capability to detect tsunamis. An increase in ocean current propagation velocity will be generated when a tsunami enters shallow water and such signature is detectable through HF coastal radar [8, 9]. A typical early warning time of 40 min can be obtained [9] for the regions covered by HF radars.

Another method for detecting tsunami waves takes advantage of ionosphere measurements. As tsunami travels over the sea, it may trigger atmospheric gravity waves, which will perturb the electron density profile in the ionosphere [10]. Such perturbations in electron density distribution are known as traveling ionospheric disturbances (TIDs). Furthermore, the tsunami-induced TIDs will lead to variations in ionospheric

4

total electron content (TEC), based on which tsunami detection can be realized. Nevertheless, other than tsunamis, several events else (e.g., mine blasts and solar flares [11]) may also be responsible for TID. Hence, this method may not be reliable and the false alarm rate may be high.

GNSS-R has been widely accepted as an efficient and accurate technique for ocean remote sensing due to its advantages in temporal and spatial coverage and immunity to weather effects [12]. Furthermore, without the cost of transmitters, the GNSS-R technique only requires small and cheap receivers, making GNSS-R-based remote sensing more accessible. These benefits of the application of GNSS-R may provide a promising solution to tsunami remote sensing. Thus, the area of interest in this thesis focuses on tsunami detection using GNSS-R signals.

1.2   Literature Review

The GNSS technology has made a significant contribution to positioning, timing and navigation. Moreover, during last two decades, it has been demonstrated that the GNSS signal is also a useful tool for remote sensing [12]. When applied for remote sensing, GNSS signals transmitted from active sources (e.g., Global Positioning System (GPS) navigation satellites) are to be received by allopatric receivers after the signals are reflected by earth surfaces (in a bistatic configuration) [13]. This technique is known as the Global Navigation Satellite System-Reflectometry.

Applications of GNSS-R in remote sensing have been investigated by a large number of researchers during the past 20 years. This technique was first proposed and applied to ocean altimetry in 1993 by Martin-Neira [14]. Following this, research

associated with GNSS-R-based ocean surface wind sensing [15–18], sea ice characterization [19–21], snow depth measurement [22, 23], soil moisture monitoring [24, 25], salinity content retrieval [26–28] and oil slick detection [29–31] has also been successfully carried out.

Since the devastating 2004 Sumatra-Andaman tsunami, progress has been made to promote GNSS-R as a new approach for deep-sea tsunami detection [5, 32, 33]. In [32], it is shown that GNSS-R altimetry is an appropriate method for tsunami detection since it is able to measure the sea surface height at a large number of regions simultaneously. The coverage of ocean areas is increased by a factor of 12 compared with a conventional altimeter [32]. The performance of GNSS-R altimetry-based tsunami detection is evaluated in [33] in terms of GNSS-R constellations. By assuming that tsunami wave anomalies greater than 20 cm can be detected, it is demonstrated that a combined GNSS constellation that consists of GPS, GLONASS and Galileo is able to detect the 2004 Sumatra-Andaman tsunami within 17 min, three times faster than the scenario where only GPS is considered. Tsunami wave parameter estimation is proceeded in [5] through modeled GNSS-R-based SSH measurement. By fully interpreting the geometry between the tsunami propagation direction and multiple GNSS signal specular reflection tracks over time, tsunami-wave propagation speed and direction and wavelength can be estimated.

Currently, the literature about GNSS-R-based tsunami detection is still limited. In summary, traditional GNSS-R tsunami detection methods are based on the GNSS-R altimetry concept. Nevertheless, it has been pointed out that the GNSS-R altimetric sensitivity of 20 cm ([5, 33]) sets a decisive limit to the detection of tsunami-induced sea surface height anomalies (SSHAs).

However, it should be noted that other than altimetry, GNSS-R technology can also be exploited as scatterometry, in which the ocean surface roughness rather than the sea level is measured. In GNSS-R scatterometry area, delay-Doppler map (DDM) is a well-known tool, from which sea surface information (e.g., roughness and wind speed) can be interpreted (more details related to DDM are discussed in Chapter 2). Furthermore, significant development on GNSS-R DDM-based sea surface sensing (e.g., [15–18, 29–31, 34–36]) has been made.

In addition, manifestations of a tsunami in the deep ocean have been investigated by a large number of researchers. In particular, tsunami-induced variations in the sea surface roughness have been reported and interpreted [6, 37, 38], therefore indicating the possibility of detecting tsunamis based upon ocean surface roughness changes. In 1996, tsunami-induced variations in the ocean surface roughness were first reported by Walker [37] and were given the name "tsunami shadow" based on observations of the darkened stripes along the tsunami front. Later, Godin [38] explained that the tsunami-induced changes in sea surface roughness are due to the tsunami-induced perturbations in sea surface wind speed. Based on these results, a theoretical model for the calculation of tsunami-induced sea surface wind velocity has been developed in [6].

From the above discussion, one can conclude that the performance of conventional GNSS-R altimetry-based tsunami detection may be corroded due to a low accuracy in SSH measurement. However, another application of GNSS-R as scatterometer is not restricted by such deterrent. This application (in which DDMs are usually utilized) has already been successfully employed in sea surface roughness sensing and wind sensing with very plausible and reliable results [16]. Furthermore, theoretical founda-

tions have been laid for the GNSS-R DDM-based deep-sea tsunami detection. With presence of a tsunami, sea surface roughness will be disturbed [6, 38]. Therefore it is believed that tsunami-induced variations in sea surface roughness, and subsequently in DDMs, may be identified and thus utilized for tsunami detection [35, 36].

1.3   The Scope of the Thesis

Based on the current statuses of the GNSS-R altimetry-based tsunami detection method, the GNSS-R DDM-based sea surface sensing missions and the theoretical basis of tsunami-induced sea surface roughness variation, a novel scheme for detecting tsunamis from GNSS-R DDMs is presented in this research. Specifically, the primary content of this thesis includes: 1) the simulation of GNSS-R DDMs of a tsunami-dominated sea surface and 2) tsunami detection and parameter estimation from such DDMs. It is also worth noting that this research focuses on deep-ocean tsunami detection. For one thing, detecting tsunamis from deep seas will provide enough time to release a warning. Another advantage is that deep-ocean detection allows a more straightforward interpretation of tsunami waves before they are reflected by the continental shelf and coastal lines [3].

The thesis is organized as following:

In Chapter 2, a detailed process for simulating tsunami-dominated sea surface DDM is proposed. The verification of the Cox and Munk model under a tsunami scenario followed by the simulation results based on the 2004 Sumatra-Andaman tsunami event is also presented. This simulation process forms the theoretical foundation of the rest of the research in this thesis.

Chapter 3 presents the new GNSS-R DDM-based tsunami detection and parameter estimation approach. The detailed steps for retrieving the SSHAs from DDMs, and particulars of the tsunami detection precept and parameter estimation are described. A preliminary verification is conducted using simulated data associated with the 2004 Sumatra-Andaman tsunami.

Chapter 4 concludes with an overview of the previous three chapters and future improvements on this research.

Chapter 2

DDM Simulation of

Tsunami-dominated Sea Surface

In this chapter, the detailed process to simulate GNSS-R DDMs of tsunami-dominated sea surfaces is presented. More specifically, the simulation process for a tsunami-free sea surface is modified for a tsunami-dominated scenario. The chapter is organized as follows: Section 2.1 introduces the theory of DDM simulation. The procedures to develop tsunami-dominant sea surface DDM are introduced in Section 2.2. In Section 2.3, the verification of the Cox and Munk model under a tsunami scenario followed by the simulation results are presented. A general chapter summary is concluded in Section 2.4.

2.1 Basics of DDM Simulation

2.1.1 Bistatic Scattering Model

GNSS-R is based upon a bistatic scattering configuration [39], in which transmitter and receiver are not collocated (see Figure 2.1). In forward scattering, the main scattering comes from the Specular Point (SP) and the area around it, which is called the Glistening Zone (GZ) [40]. The position of SP can be determined from the geometry of the transmitter and the receiver since the incident and scattering angles are equal on SP. Usually, the area of GZ is about 200 km square [13].

The received signal can be considered as a superposition of scattering components from different points on the GZ. Each component has its corresponding delay and Doppler shift, which are caused by different path lengths and the relative motions of the transmitter, the receiver and the scattering point, respectively. In other words, every point on the GZ can be represented by delay and Doppler shift. Therefore, each GZ point in space with a pair of delay-Doppler values can be mapped to a new domain that is characterized by delay and Doppler shift, known as delay-Doppler (DD) domain. GNSS-R data are typically mapped and processed in such domain, and in the fashion of the so-called delay-Doppler Maps (DDMs) [40].

A theoretical model, known as the Z-V model [41], is commonly used to model the GNSS-R scattering and simulate DDMs. The Z-V model depicts the scattered GNSS signal power as a function of delay and Doppler shift and is in the following form

$$\left\langle |Y(\Delta\tau, \Delta f)|^2 \right\rangle = T_i^2 \iint_A \frac{D^2(\vec{\rho})\sigma^0(\vec{\rho})\Lambda^2(\Delta\tau)|S(\Delta f)|^2}{4\pi R_R^2(\vec{\rho})R_T^2(\vec{\rho})} d^2\rho, \tag{2.1}$$

11

where

$\langle |Y(\Delta\tau, \Delta f)|^2 \rangle$	power of received signal;
$\vec{\rho}$	the position vector of observed surface point with respect to SP;
$\Delta\tau = \tau(\vec{\rho}) - \tau$	τ and $\tau(\vec{\rho})$ are the delays at SP and the observed surface point, respectively;
$\Delta f = f_d(\vec{\rho}) - f_d$	f_d and $f_d(\vec{\rho})$ are the Doppler shifts at SP and the observed surface point, respectively;
T_i	the coherent integration time;
D	antenna radiation pattern;
R_T	the distance from the transmitter to a point on the ocean surface;
R_R	the distance from the receiver to a point on the ocean surface;
σ^0	dimensionless scattering coefficient;
A	scattering surface, approximately the GZ.

In addition, the triangular pulse function Λ is defined as

$$\Lambda(\Delta\tau) = \begin{cases} 1 - \left|\frac{\Delta\tau}{\tau_c}\right| , & -\tau_c \leq \Delta\tau \leq \tau_c \\ 0 , & \text{otherwise} \end{cases} \tag{2.2}$$

where $\tau_c = 1/1023$ ms is the length of a chip of the coarse/acquisition (C/A) code.

Transmitter

iso-Doppler line

iso-delay line

Receiver

SP

100

50

0 Ambiguity-free
line

50

y (km)

100

50

0

50

100

x (km)
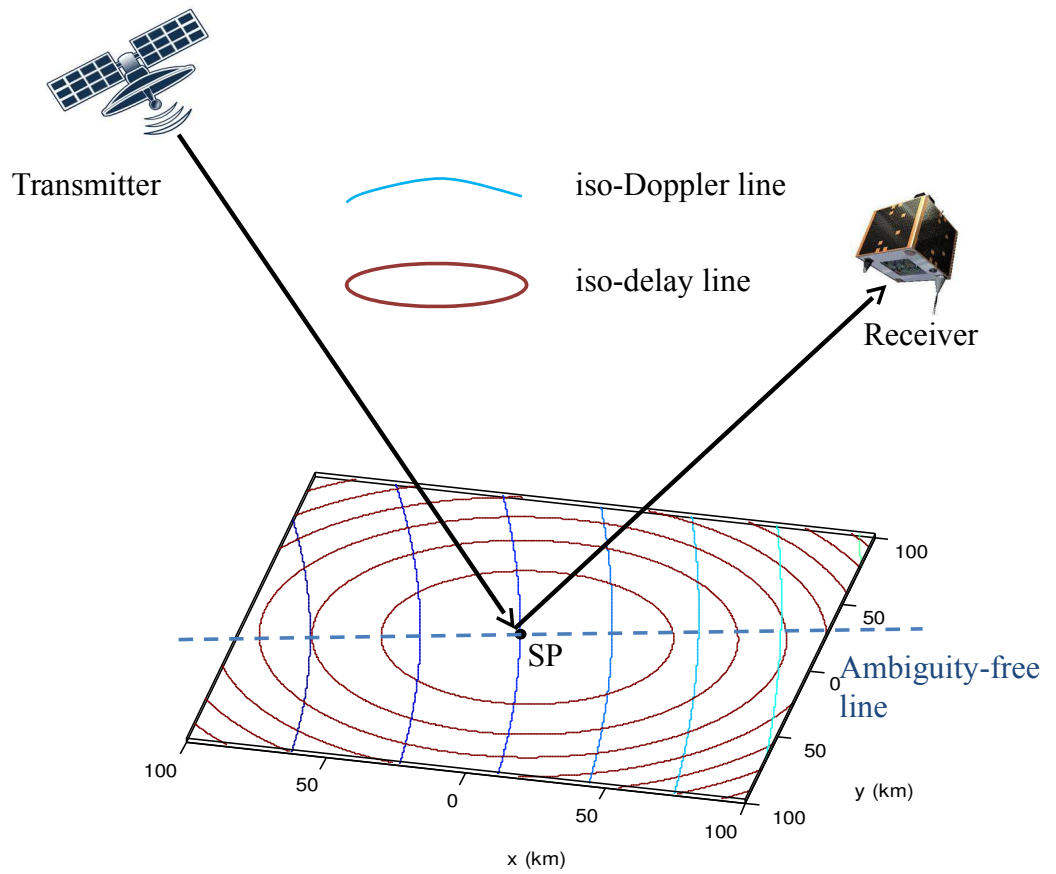
Figure 2.1: A schematic of the GNSS-R geometry, with a transmitter and a receiver as well as iso-range and iso-Doppler lines on GZ.

On the other hand, the function $S(\Delta f)$ is defined as

$$S(\Delta f) = \sin(\pi T_i \Delta f)/(\pi T_i \Delta f). \tag{2.3}$$

According to equation (2.1), in order to accomplish the DDM simulation, the position and area of GZ are to be determined first. Afterwards, coordinate transform needs to be processed since GZ points are actually on the spherical earth surface. For details of these two specific steps, refer to [42]. Then the power distribution in spatial domain will be mapped to DD domain. For illustration purposes, the relationship between spatial clusters and DD cell is presented in Figure 2.2. It can be noticed that each DD cell is associated with two separate spatial clusters. This will not bring problem in the DDM simulation stage. However, it will cause an ambiguity issue in retrieval procedure (investigated in Chapter 3), where mapping signal power/scattering coefficient from DD to spatial domains is processed.
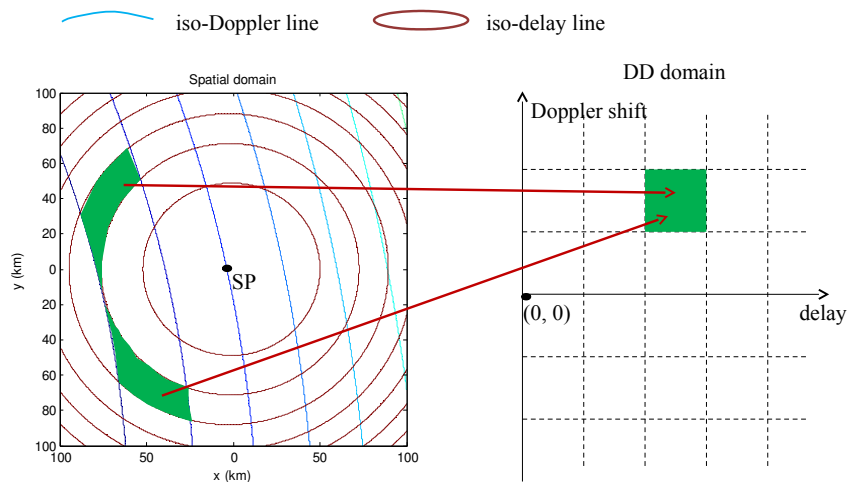
Figure 2.2: Relationship between spatial clusters and DD cells.

2.1.2 Sea Surface Model

The power received from each grid element is dependent on its scattering coefficient [42]. Moreover, with the exception of σ^0, the rest of the terms in equation (2.1) are usually known for a specific GNSS system and its geometry. Therefore, the scattering coefficient σ^0 is specifically investigated here, and it can be written as [41]

$$\sigma^0(\vec{\rho}) = \pi|\Re|^2 P(-\frac{\vec{q}_\perp}{q_z})(\frac{|\vec{q}|}{q_z})^4, \tag{2.4}$$

where $|\Re|^2$ is the Fresnel reflection coefficient that depends on the local elevation angle, polarization and the complex dielectric constant of sea water [39]; the scattering vector $\vec{q} = \vec{q}_\perp + q_z\hat{z}$ can be obtained with the locations of the transmitter, receiver and corresponding surface point; $-\frac{\vec{q}_\perp}{q_z}$ is the ocean surface slope, denoted hereafter as $\vec{s}$. $P(\vec{s})$ is the slope Probability Density Function (PDF) of the ocean surface gravity wave, which is believed to be subject to Gaussian distribution with wind-dependent upwind variance σ_u^2 and crosswind variance σ_c^2 [39]. It is worth mentioning that tsunami waves are gravity waves. $P(\vec{s})$ is expressed as [18]

$$P(\vec{s}) = \frac{1}{2\pi\sqrt{\det(W)}} \exp[-\frac{1}{2}\begin{pmatrix} s_x \\ s_y \end{pmatrix}^T W^{-1} \begin{pmatrix} s_x \\ s_y \end{pmatrix}] \tag{2.5}$$

where s_x, s_y represent the surface slope components on the x and y axes, and

$$W = \begin{bmatrix} \cos\phi_0 & -\sin\phi_0 \\ \sin\phi_0 & \cos\phi_0 \end{bmatrix} \times \begin{bmatrix} \sigma_u^2 & 0 \\ 0 & \sigma_c^2 \end{bmatrix} \times \begin{bmatrix} \cos\phi_0 & \sin\phi_0 \\ -\sin\phi_0 & \cos\phi_0 \end{bmatrix}, \tag{2.6}$$

where ϕ_0 is the angle between the wind direction and the x-axis.

15

As mentioned above, the sea surface scattering coefficient is dependent on sea surface slope. In fact, the clean sea surface mean square slope model of Cox and Munk [43] substantiates an empirical relationship between the wind speed (WS) at the height of 10 m above the sea surface (U_{10}) and the sea surface mean square slope (MSS). Furthermore, an empirical modification made on this model [44] is adopted in this thesis to assure this model better fits GNSS signals. The modified clean sea surface mean square slope model of Cox and Munk [43] is in the following form

$$\sigma_u^2 = 0.45 \times (3.16 \times 10^{-3} f(U_{10}))$$
$$\sigma_c^2 = 0.45 \times (0.003 + 1.92 \times 10^{-3} U_{10}) \tag{2.7}$$

where

$$f(U_{10}) = \begin{cases} U_{10} & U_{10} \leq 3.49 \\ 6 \cdot \ln(U_{10}) - 4 & 3.49 < U_{10} \leq 46 \\ 0.411 \cdot U_{10} & U_{10} > 46 \end{cases} \cdot \tag{2.8}$$

In summary, with the knowledge of U_{10} the corresponding scattering coefficient can be simulated via the Cox and Munk model. Moreover, with the sea surface scattering coefficient distribution the associated DDM can be simulated base upon the Z-V model.

2.2 Tsunami-dominant Sea Surface Scenario

By following the steps presented in Section 2.1, DDMs can be readily simulated with the knowledge of U_{10} for a tsunami-free sea surface, based on the Cox and Munk model [43] and the Z-V model [41]. With this in mind, the associated DDM simulation under a tsunami scenario can be completed if the distribution of U_{10} over

a tsunami-dominant sea surface is available.

For a tsunami-dominant sea surface, the effective wind speed (WS_{eff}) can be derived from the tsunami-induced wind speed perturbation model [6], i.e., the so-called Godin model. This model was proposed based on the observation data of "tsunami shadow" from the October 4, 1994 Hokkaido tsunami [37]. The theoretical derivation of this model and its validation based on simulation are presented in [6]. Moreover, this model has been successfully applied in the simulation of radar backscattering strength over a tsunami region (e.g., [6, 7]). The tsunami-induced variations in radar backscattering strength estimated based on the Godin model are consistent with the Jason-1 measurement [6]. Thus, the Godin model is employed here to determine the effective wind speed during a tsunami period. This model shows that the effective wind speed during a tsunami event depends on tsunami parameters and differs from the background wind speed (WS_0) by a factor of M [6], and

$$M = 1 - \frac{\kappa a c}{H u_* \ln \beta} \tag{2.9}$$

where $\kappa = 0.4$, $u_* = 0.04 U_{10}$, H is the height of the background logarithmic boundary layer, a is the sea surface height change due to tsunami, $c = \sqrt{gD}$ is the tsunami propagation velocity, where g is the acceleration due to gravity, D is the depth of sea, and

$$\beta = \frac{\kappa u_* T_0}{2 \pi z_0}, \tag{2.10}$$

where $z_0 = 0.01 u_*^2 / g$ represents the roughness length, and T_0 is tsunami period.

Equations (2.9) and (2.10) represent the Godin model [6]. By integrating the Godin model with the combination of the Z-V model and the Cox and Munk model, the tsunami DDMs can be simulated with different tsunami parameters and WS_0.

17

2.3   Simulation Results

In this section, feasibility of the Cox and Munk model under a tsunami scenario is tested first. Then, the parameters associated with tsunami DDM simulation are set. After that, the tsunami DDM simulation results are presented.

2.3.1   Feasibility of the Cox and Munk Model under a Tsunami Scenario

The Jason-1 satellite altimeter encountered the tsunami on the morning of December 26, 2004 [6] (shown in Figure 2.3, this graphic is modified from the work of the National Geophysical Data Center/NOAA, at http://www.ngdc.noaa.gov/hazard/img/ 2004_1226.jpg)). It recorded radar backscattering coefficient and sea surface wind speed, thereby offering an opportunity to study the wind speed and σ^0 during the tsunami event. Before exerting the tsunami DDM simulation, the feasibility of the Cox and Munk model under a tsunami event should be examined. By employing the Cox and Munk model, the σ^0 of a tsunami-dominant sea surface can be simulated with the knowledge of U_{10} over the corresponding region. Based on this, a comparison between the Jason-1 measured σ^0 and the simulated σ^0 can be made.

Figure 2.4(a) illustrates the Jason-1 measured sea surface wind speeds (solid line) over the range of (6.00°S, 83.60°E) to (4.99°N, 87.54°E) with the presence of the tsunami leading wave front. For the simulation, some assumptions are made below:

1) The GNSS-R transmitter, receiver and the SP are set on the same line that is also perpendicular to the sea surface.
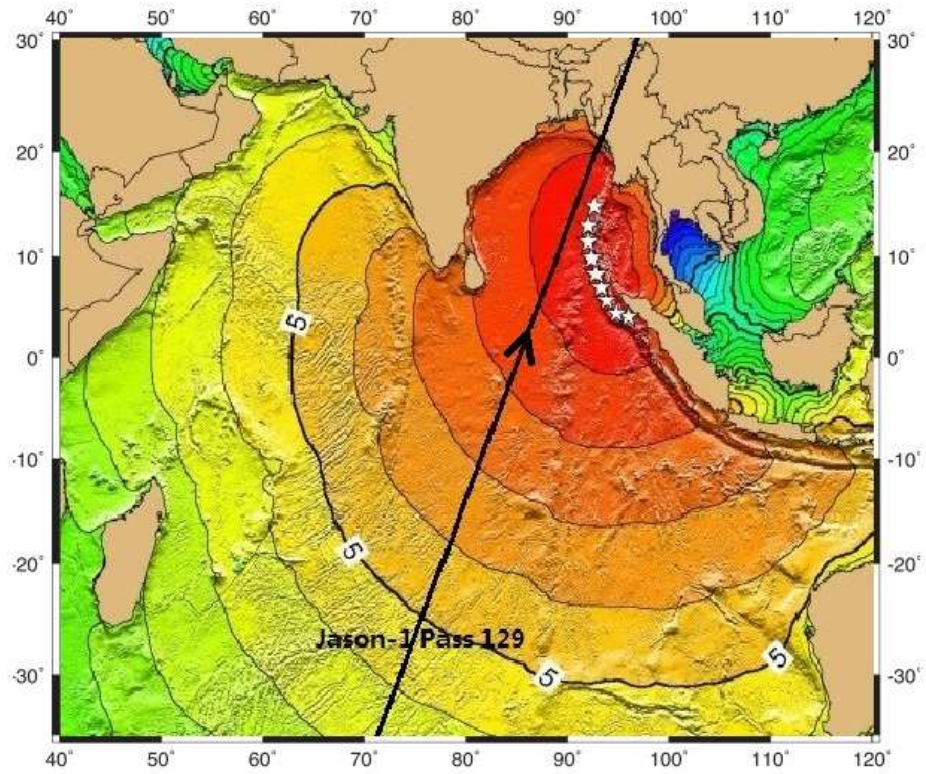
Figure 2.3: Jason-1 satellite altimeter ground track during the 2004 Sumatra-Andaman tsunami. Black line indicates the Jason-1 ground track with a direction in accordance with the arrow. White stars represent the epicentre. Contours of the tsunami leading front are also shown with hourly intervals.

19

2) The SP follows the Jason-1 ground track.

3) The Jason-1 measured U_{10} is uniform along tsunami wave front.

The first assumption is required to simulate the Jason-1 backscattering scenario. The second assumes that the GNSS-R system and Jason-1 monitored this region at the same time. The last one aims at forming a two-dimensional wind speed distribution over the glistening zone.

The size of GNSS-R glistening zone is about 200 km by 200 km. Through inputting the wind speeds that are interpolated using the Jason-1 measured U_{10} over sea surface, the scattering coefficient can therefore be simulated. Here, only the σ^0 at SP which follows the Jason-1 ground track is recorded and compared with the Jason-1 measurements. Figure 2.4(b) shows the σ^0 measured by Jason-1 and the σ^0 simulated by the Cox and Munk model. A good consistency between the measured σ^0 and the simulated σ^0 can be observed with a correlation coefficient of 0.93. In Figure 2.4(b), the simulated scattering coefficients for GNSS-R seem to be slightly overestimated than the measurement by Jason-1. This is mainly due to the difference in the operating frequencies of GNSS-R (1.5 GHz, i.e., L-band) and Jason-1 (5.4 GHz, i.e., C-band). The average difference of the scattering coefficient is about 1.33 dB and this is consistent with the analysis in [45], where the difference of σ^0 between L- and C-band measurements is found to be about 2 dB. Therefore, the feasibility of the Cox and Munk model on the tsunami DDM simulation is confirmed.
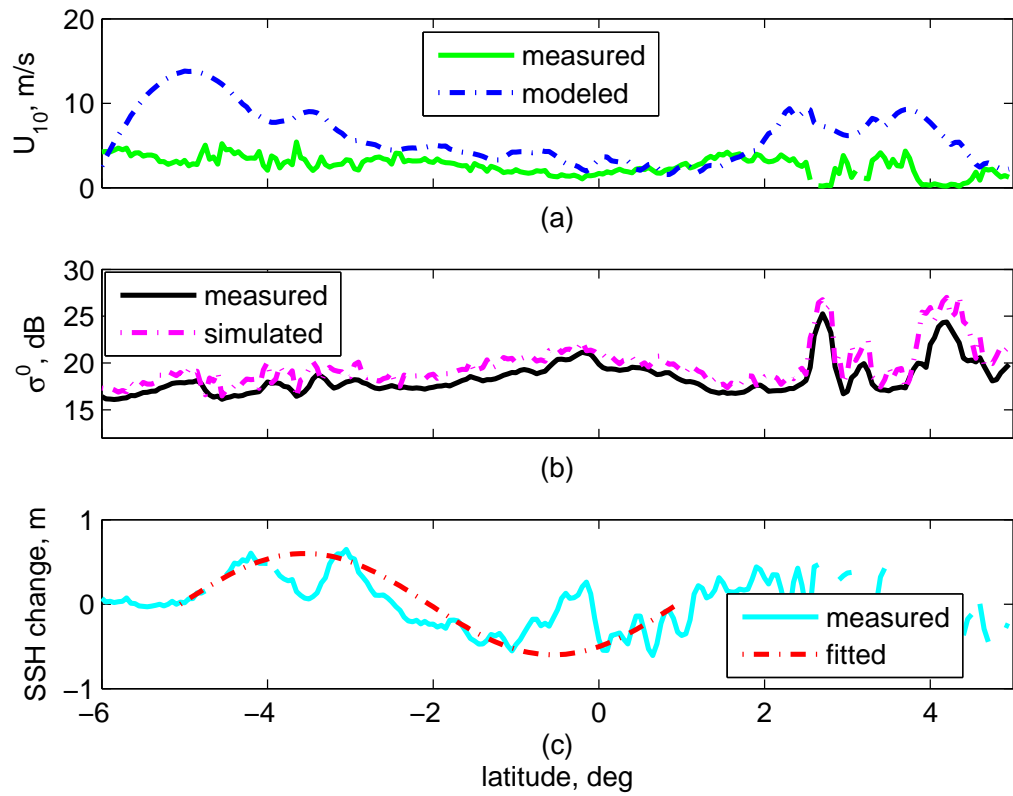
Figure 2.4: Jason-1 measurement for pass 129 from (6.00°S, 83.60°E) to (4.99°N, 87.54°E) obtained during the 2004 tsunami: (a) Sea surface U_{10}, (b) Backscattering coefficient σ^0, and (c) SSH change due to a tsunami. Gaps in the curves are caused by deficiency of measured data.

2.3.2 Simulation Scenario Parameters

Based on the analysis above, it can be concluded that the σ^0 of a tsunami-dominant sea surface can be simulated via the Cox and Munk model [43]. Thus, the tsunami DDMs can be simulated through the Z-V model [41], the Cox and Munk model [43] and the Godin model [6] with reliability.

Here, to facilitate the simulation, the typical empirical values are adopted in align with those in [6], i.e., $T_0 = 40$ min, $D = 4000$ m and $H = 60$ m. If the SSH change a due to tsunami and the background wind speed are known, the effective wind speed over a tsunami surface can therefore be determined by implementing the Godin model.

The SSH measured by Jason-1 on cycle 109 during the tsunami event is subtracted by the average SSH observed over the exactly same ground track on cycles 108 and 110, and the difference is regarded as tsunami-induced SSH change a (shown in Figure 2.4(c)). This process is in accordance with [46]. Besides, it has been reported in [46] that the tsunami-induced SSH change a over the range from (5.00°S, 83.96°E) to (1.00°N, 86.12°E) can be well fitted by a sine wave with a wavelength of 580 km and an amplitude of 60 cm, as shown by a dash line in Figure 2.4(c). Alternatively, the sine model is treated as another form of input a for reference. In addition, a is assumed to distribute uniformly along the contours of the tsunami leading wave front, which are concentric circles with a center at the epicenter (3.4° N, 94.2° E).

The U_{10} over the region under investigation measured by QuikSCAT on its orbit 28744 is considered to be the background wind speed, shown in Figure 2.5. The data was recorded around 45 min before the earthquake appeared, which means this measurement is totally free of the tsunami influence. Therefore, it is reasonable to use

the QuikSCAT measurement as the background U_{10}. The effective U_{10} is calculated using only the QuikSCAT measurement over the Jason-1 ground track and is shown in Figure 2.4(a). Difference between the modelled and measured wind speeds can be seen in Figure 2.4(a). This is because the modelled wind speed significantly relies on the background wind speed (i.e., before the appearance of tsunami). The only available background wind speed data of the region under investigation, immediately before the tsunami, was measured by QuikSCAT. However, the data was collected 45 min before the earthquake happened. Moreover, Jason-1 flew over the same region 115 min after the earthquake appeared. Thus, a time gap of 160 min exists between the measured and the modelled wind speeds. As known to all, wind speed may change significantly after two hours. This may explain the difference between the modelled and measured wind speeds. Furthermore, with a closer observation of Figure 2.5 a storm seems to exist in the background wind speed (the region enclosed by black lines). Due to high dynamics of a storm, it could have disappeared before the following Jason-1 measurement. This also can account for some of biases.

The parameters mentioned above are tabulated in Table 2.1. In terms of GNSS-R simulation scenario, the parameters are kept the same as those in [31], also shown in Table 2.1.

In order to manifest a unique influence of the tsunami on GNSS-R sea surface remote sensing in this work, a continuous detection over a fixed region is assumed. To achieve this, both of the transmitter and the receiver are set fixed over time. In this fashion, the variations caused by the geometry change of GNSS-R system will be eliminated as well, which allows a more direct observation of tsunami effect. The region of our interest is set around (6.0081° S, 83.6019° E) with a size of 200 km by
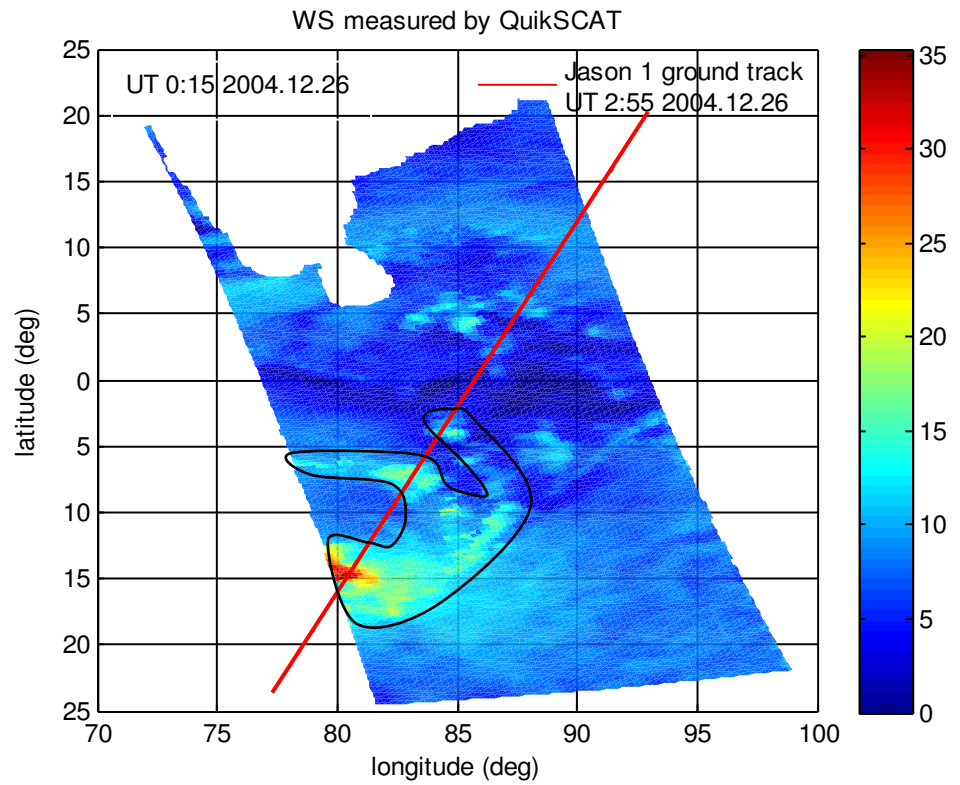
Figure 2.5: Wind speed distribution measured by QuikSCAT 45 min ahead of the appearance of the earthquake.

Table 2.1: Tsunami DDM Simulation Setting Up

Simulation parameters	Value (Data source)
Tsunami period (T_0)	40 min
Depth of ocean (D)	4000 m
Height of the background logarithmic boundary layer (H)	60 m
SSH change (a)	Jason-1 measurement/ Fitted sine wave model
Background wind speed	QuikSCAT measurement on orbit 28744
Receiver height	680 km
Transmitter velocity	(-2.72, 2.68, -.65) km/s
Receiver velocity	(7.21, 1.23, 1.72) km/s
Spatial grid size	400×400 m^2
SP position	(6.0081° S, 83.6019° E)

200 km. The first simulation result was conducted for 02:55:22 UT. The study region at this time was tsunami-free. Therefore, this first simulation result is considered as the initial baseline for the following results. Meanwhile, the SSH change in Figure 2.4(c) is regarded as initial distribution. The initial simulation only depends on the background U_{10} over this region measured by QuikSCAT. However, within a few minutes, this region experienced a tsunami passage. The tsunami-induced wind speed perturbation model must be employed with the tsunami entering into this region. The effective U_{10} will be calculated based on this model with the knowledge of background U_{10} and a.

As we have assumed $D = 4000$ m, the tsunami propagation speed can thus be approximated by 200 m/s. Meanwhile, the initial distribution of a over space is known. For this reason, the a over this region at each moment can be easily deduced according to the distance and tsunami propagation speed. Then, the effective U_{10} at different periods can also be determined.

2.3.3   Results

The spatial distribution of tsunami-induced SSH change based on a sine wave model is shown in Figure 2.6.

Figure 2.7 displays the simulated σ^0 by adopting the fitted sine wave model as input a. The time gaps between the initial detection in Figure 2.7(a) and those from Figure 2.7(b) to Figure 2.7(f) are: 9.17 min, 22.92 min, 36.67 min, 50.42 min and 64.17 min, respectively. Figure 2.8 shows the simulated DDMs corresponding to the scattering coefficient maps in Figure 2.7.
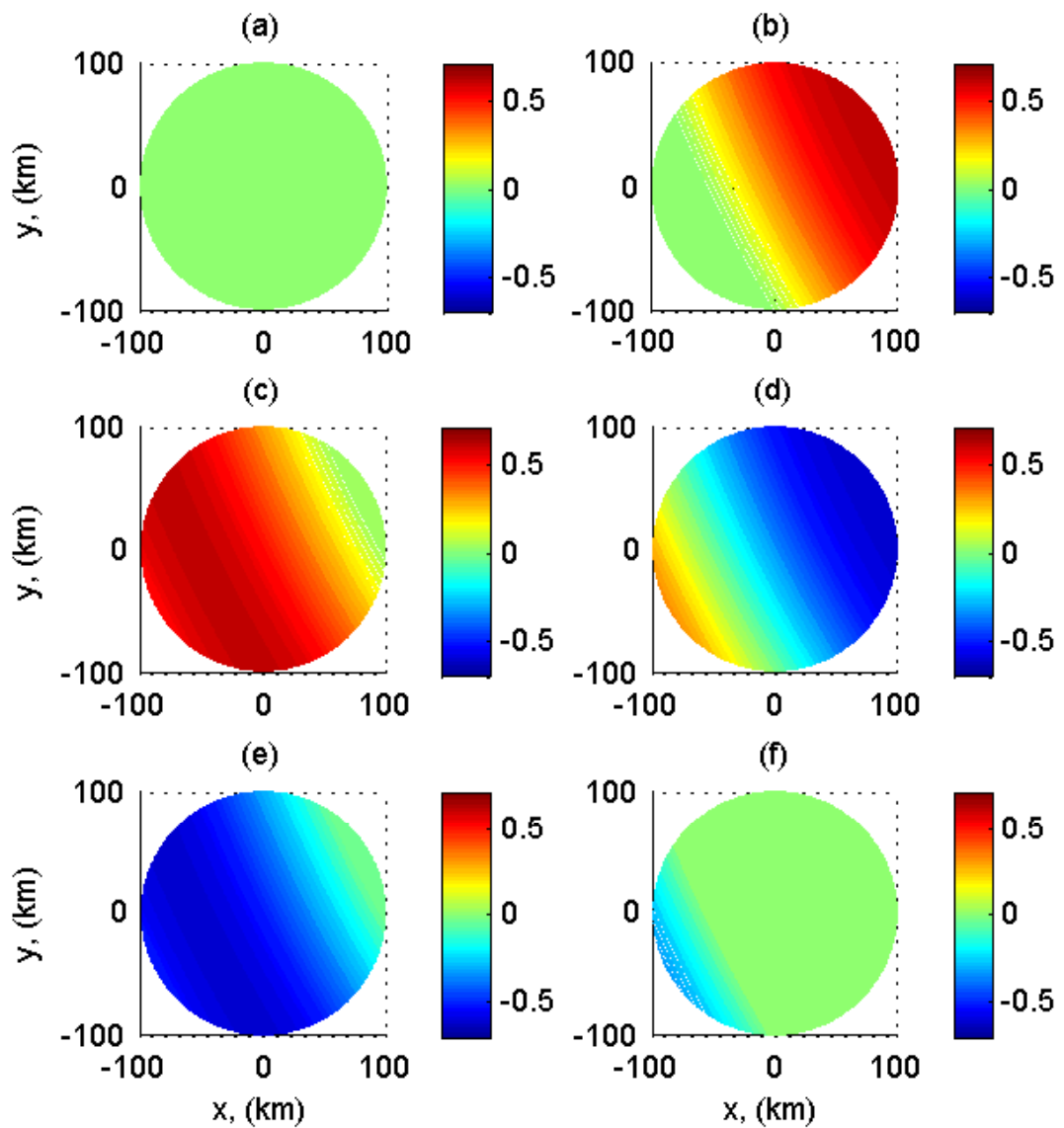
Figure 2.6: Spatial distribution of tsunami-induced SSH change based on a sine wave model: (a) before tsunami; and with (b) a part of tsunami leading front, (c) the tsunami crest, (d) a part between the crest and trough, (e) the tsunami trough, and (f) the tail of tsunami leading front.
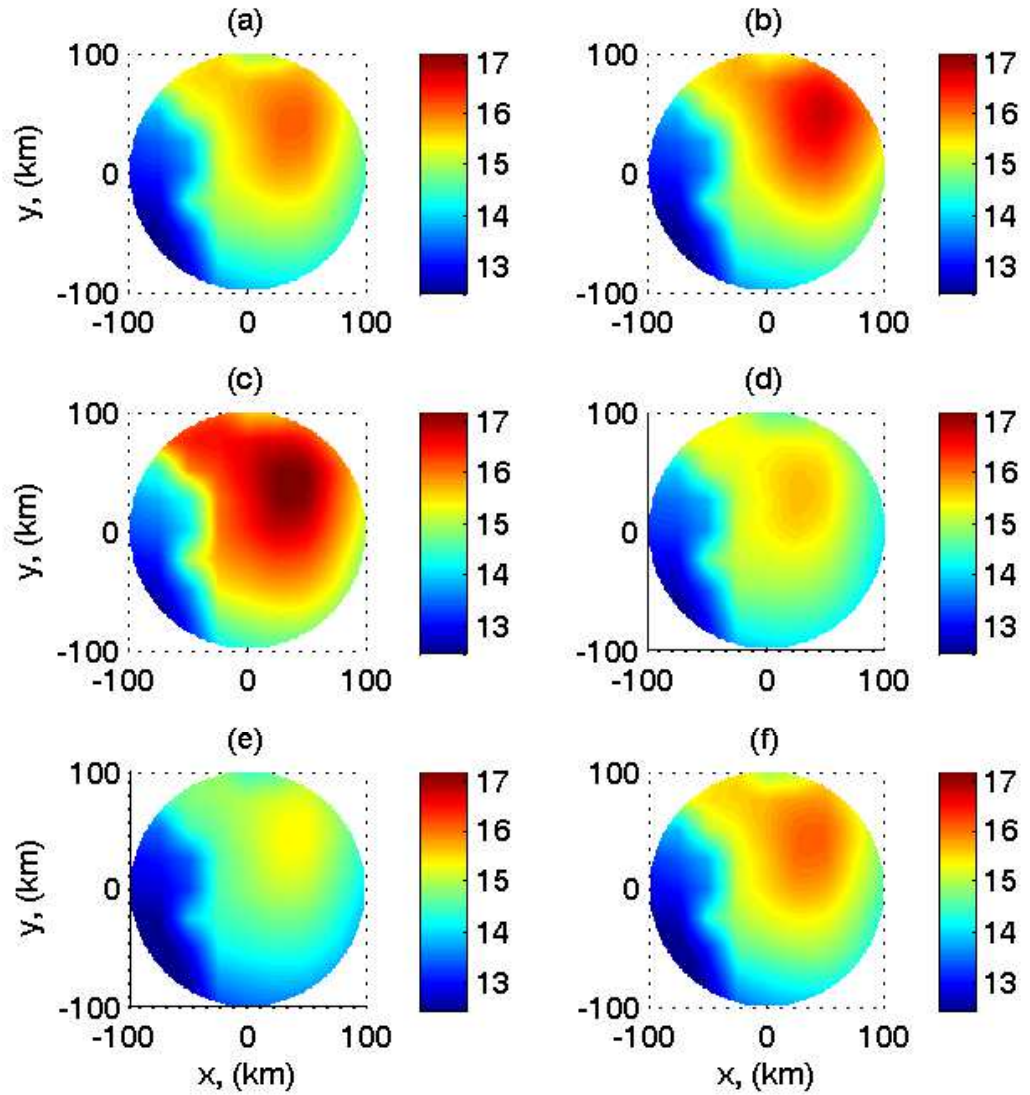
Figure 2.7: Simulated σ^0 using fitted sine wave as input: (a) without tsunami; and with (b) a part of tsunami leading front; (c) the tsunami crest; (d) a part between the crest and trough; (e) the tsunami trough; and (f) the tail of tsunami leading front. The arrow indicates the tsunami propagation direction.

In order to manifest the tsunami-induced variations in σ^0 and DDMs, the simulation results with tsunami are subtracted by the initial result that contains no tsunami, i.e., sub-plots (b) - (f) in both Figure 2.7 and Figure 2.8 are subtracted by the corresponding sub-plot (a). The resultant scattering coefficient and DDM differences are displayed in Figure 2.9 and Figure 2.10, respectively. Although the overall shapes in each subplot of Figure 2.7 or Figure 2.8 are similar, variations still can be observed. From Figure 2.9, the σ^0 variations caused by the tsunami are found to be about ± 1 dB. This result is consistent with the analysis in [6].

Intuitively, an increase in a will lead to a reduction in M factor according to (2.9). On the other hand, a decrease in U_{10} will contribute to an increase in σ^0. On the whole, the variations in σ^0 are coincident with the changes of a. Therefore, the passage of the tsunami can be identified from Figure 2.9: (a) the leading front appears first; (b) then comes the crest; (c) the transition region between the crest and the trough approaches later; (d) after that, the trough emerges; (e) finally, the tsunami wave propagates out of this region with only a small portion of the tail remaining. The variations in σ^0 are approximately proportional to the tsunami-induced SSH changes. The tsunami-induced variations in DDMs can be observed in Figure 2.10.

The spatial distribution of tsunami-induced SSH change based on Jason-1 measurements is shown in Figure 2.11. Since the tsunami-induced variations in simulated σ_0 maps and DDMs are not so obvious, only the differences between the results with and without tsunami are displayed in Figures 2.12 – 2.13. Due to the non-ideal-sine distribution of measured a, these simulation results differ slightly from those based on fitted sine wave input a. However, with a closer observation of Figure 2.12, the variations in σ^0 are also consistent with the distribution of measured a.

29
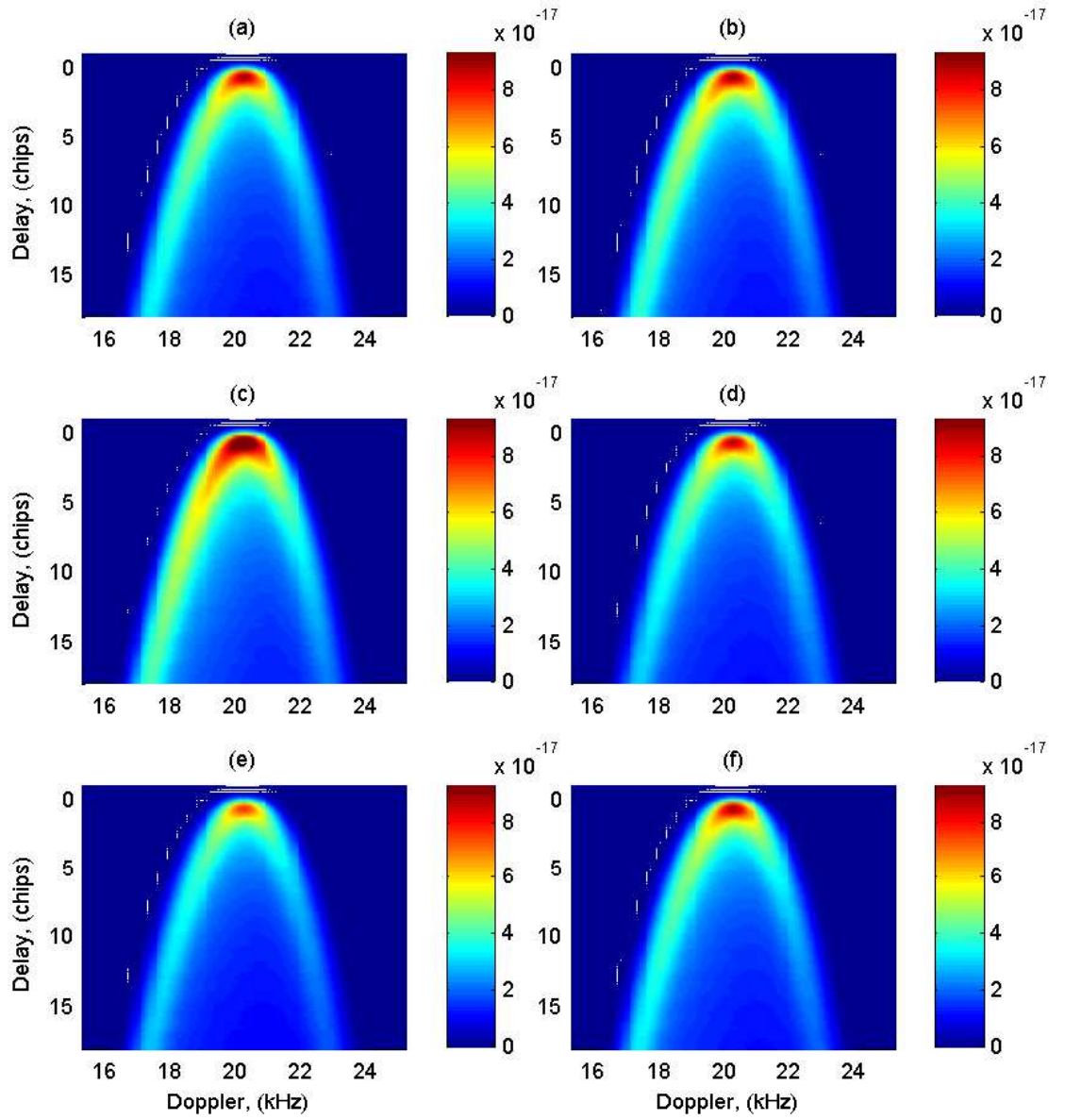
Figure 2.8: Corresponding DDMs resulting from σ^0 in Figure 2.7.
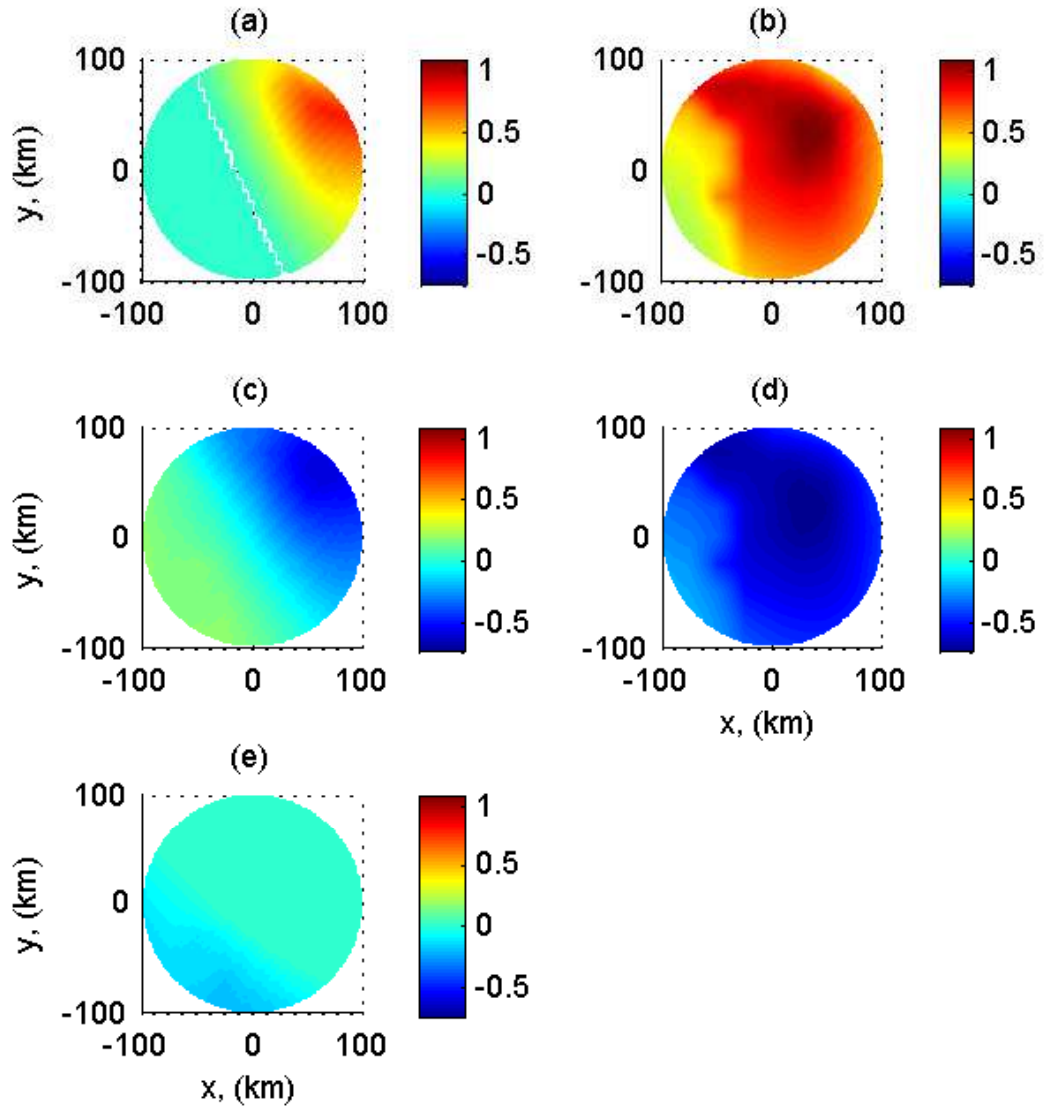
Figure 2.9: Differences of the scattering coefficients of tsunami-dominated and tsunami-free sea surfaces (based on sine wave-modelled SSH changes).
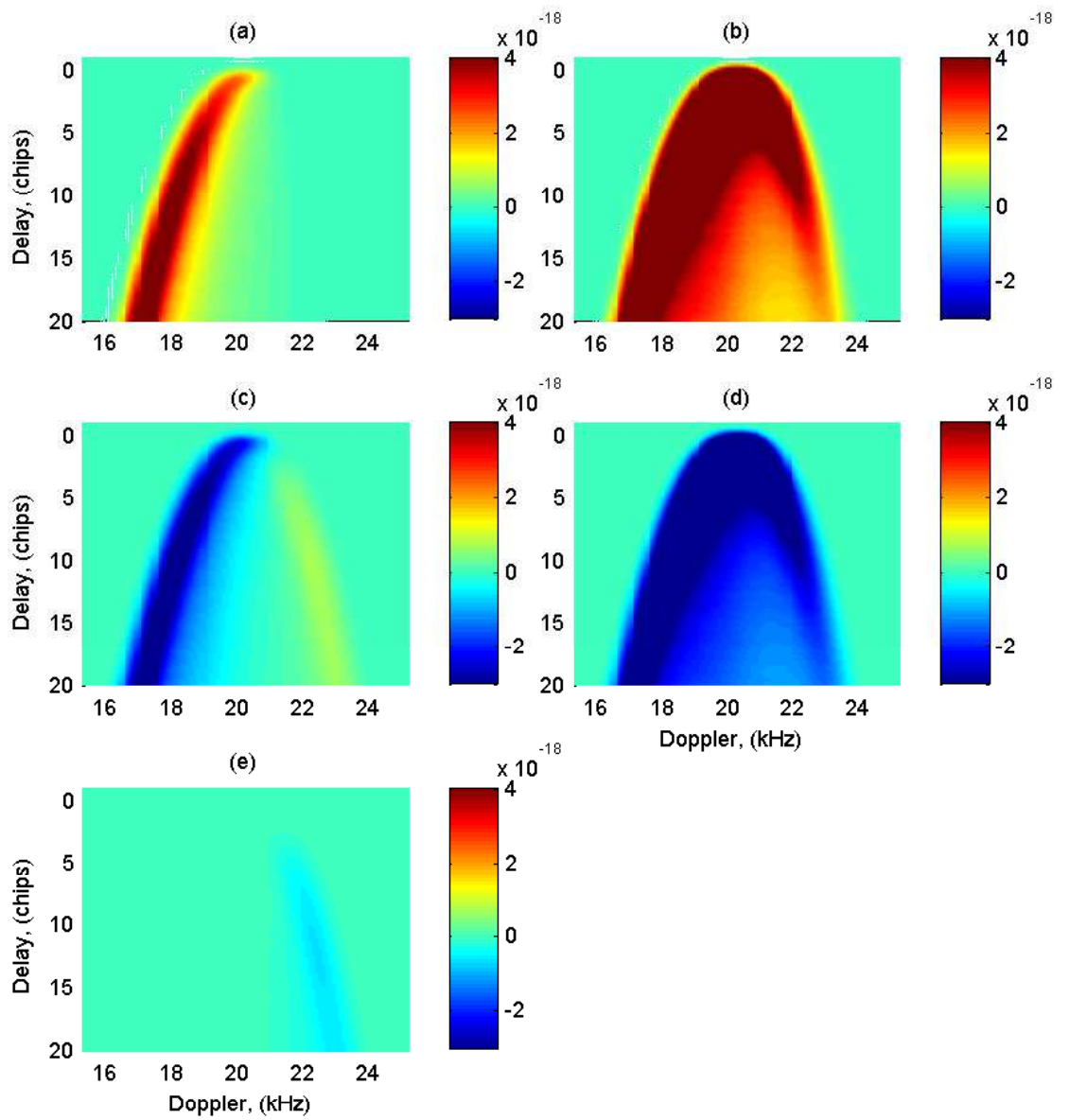
Figure 2.10: Differences of the DDMs of tsunami-dominated and tsunami-free sea surfaces (based on sine wave-modelled SSH changes).

32
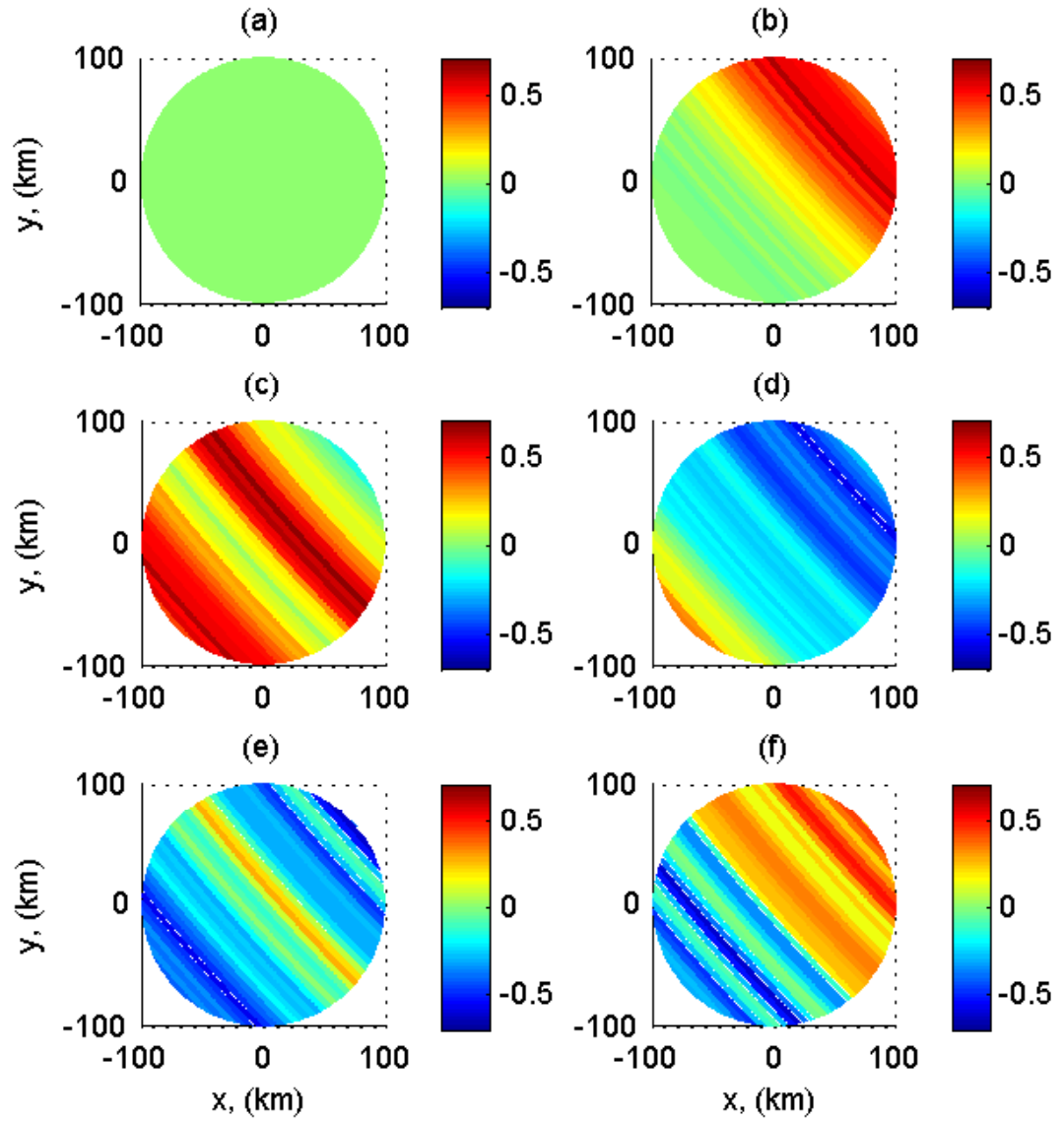
Figure 2.11: Spatial distribution of tsunami-induced SSH change based on Jason-1 measurements.
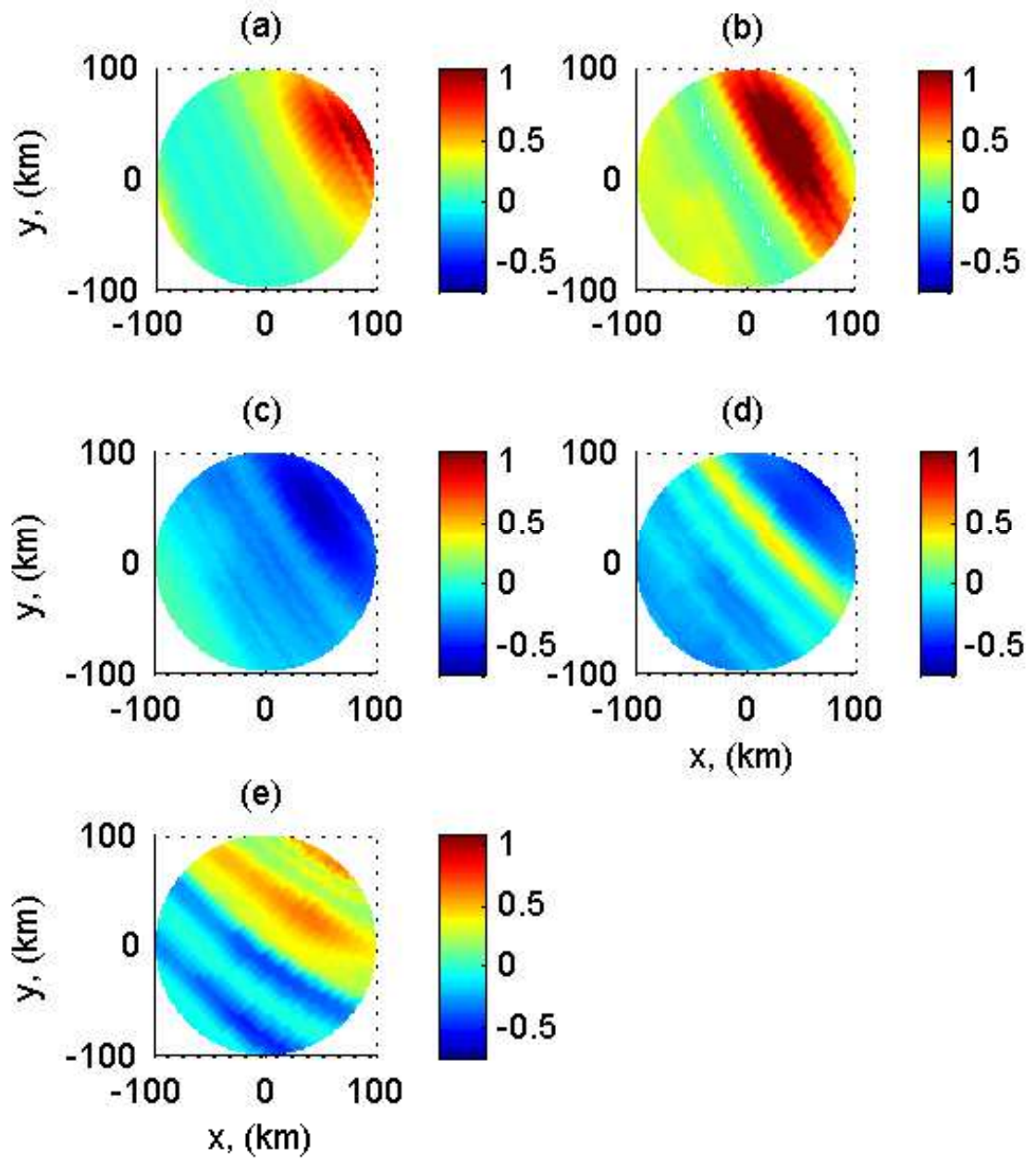
Figure 2.12: Differences of the scattering coefficients of tsunami-dominated and tsunami-free sea surfaces (based on Jason-1 measured SSH changes).

34
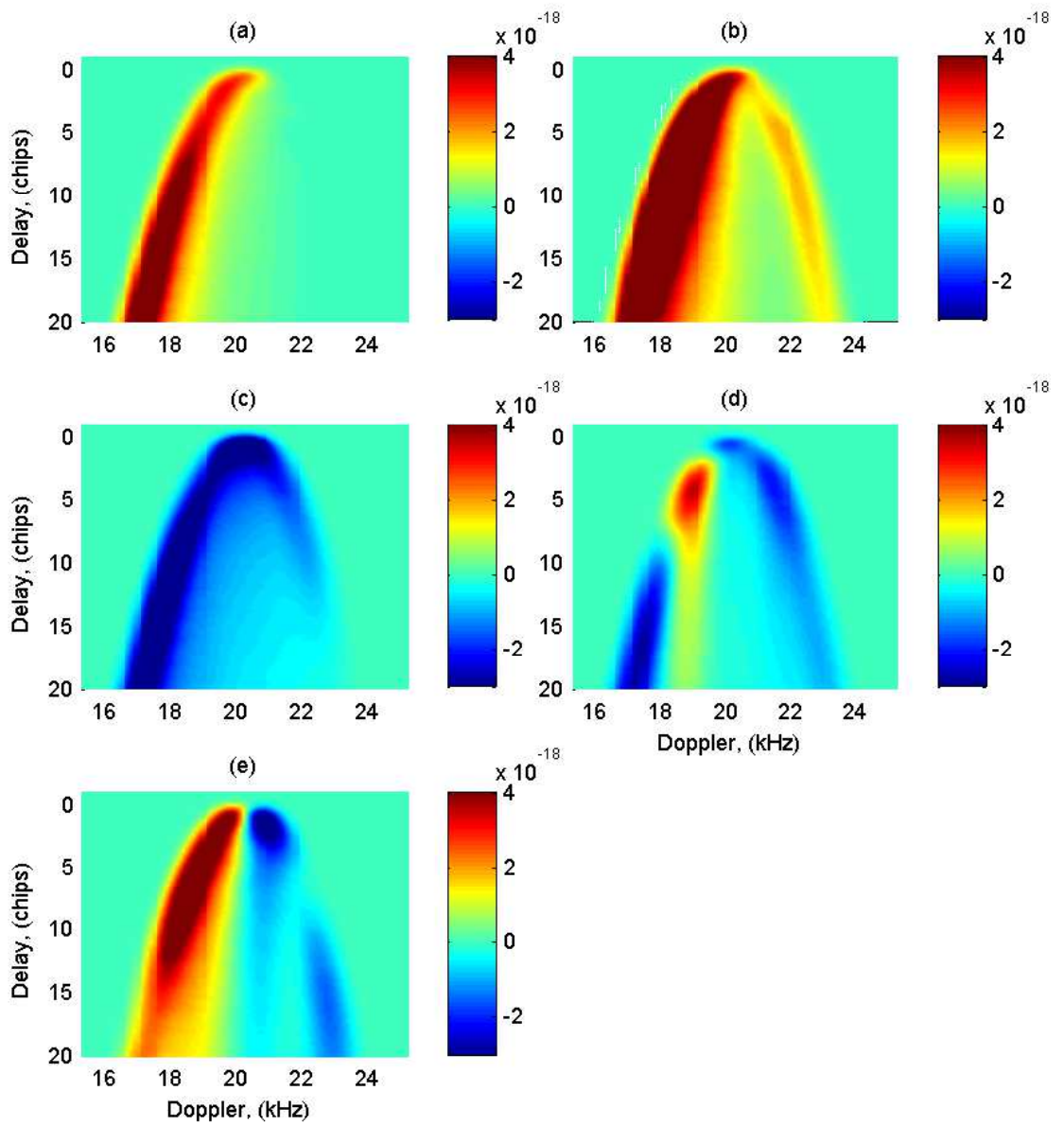
Figure 2.13: Differences of the DDMs of tsunami-dominated and tsunami-free sea surfaces (based on Jason-1 measured SSH changes).

2.4 General Chapter Summary

In this chapter, a process is proposed to simulate the DDM of a tsunami-dominant sea surface. The Z-V model, the Cox and Munk model and the tsunami-induced wind speed perturbation model are employed in this method. The feasibility of Cox and Munk model under the tsunami scenario is confirmed (A correlation coefficient of 0.93 between the simulated and measured σ^0 is observed). After verifying its applicability, σ^0 and DDMs are simulated with two different tsunami-induced SSH change inputs, i.e., Jason-1 measurement and fitted sine wave model. The σ^0 variations caused by the tsunami are found to be about ± 1 dB, which is consistent with the result in [6]. Finally, by studying the tsunami-induced variations in σ^0, the passage of tsunami can be identified. In the next chapter, the tsunami-dominated sea surface DDM simulation technique is applied for tsunami detection and parameter estimation approach development.

Chapter 3

Tsunami Detection and Parameter Estimation From GNSS-R DDM

In this chapter, a scheme to detect tsunamis and estimate tsunami parameters from GNSS-R DDM is developed. In Section 3.1, the procedures and principles associated with the determination of tsunami-induced SSHAs from DDMs are demonstrated. In Section 3.2, a precept and corresponding criteria for tsunami detection are described. The tsunami parameter estimation is investigated in Section 3.3. Results are presented in Section 3.4. Section 3.5 concludes with an overview of the work in this chapter.

3.1 Model Description and Retrieval Implementation

The work presented in Chapter 2 has illustrated the tsunami-induced variations in both σ^0 distribution and DDMs, from which the passage of a tsunami can be identified. Because of this, GNSS-R DDM has appeared as a promising solution to tsunami detection [35]. In essence, sea surface wind speed will be perturbed when a tsunami occurs [6, 38]. As a result, the scattering coefficients σ^0 distribution will vary due to a tsunami, as σ^0 is dependent on the WS.

A full scheme for deriving the tsunami-induced SSHA from DDMs is developed here based on the Z-V bistatic scattering model [41], the Cox and Munk model of sea surface mean square slope [43] and the tsunami-induced wind perturbation model [6]. Scattering coefficients σ^0 are to be retrieved from DDMs first. Next, the WS distribution is recovered from the σ^0. After that, the tsunami-induced SSHA can be determined from the retrieved WS. In order to implement this step all DDMs are assumed to be of tsunami-dominant sea surface. False alarms derived from this assumption will be eliminated by a later tsunami detection procedure (see more details in Section 3.2).

3.1.1 Scattering Coefficient Retrieval

DDMs that depict scattered GNSS signal power over two-dimensional (2-D) space in terms of delay offsets ($\Delta\tau$) and Doppler shifts (Δf) can be simulated using the Z-V model [41]. To substantiate the tsunami surface characteristics, the scattering

coefficient distribution in the spatial domain needs to be retrieved from DDMs in the first stage. Two approaches in the literature, specifically the Jacobian approach [47] and the spatial integration approach (SIA) [41], are applicable for σ^0 retrieval from DDMs. The main distinction between these two methods lies in the way they accomplish calculation, i.e., the Jacobian approach uses a change in variables from spatial to DD domains ahead of the calculation, while the SIA does not [30]. It has been demonstrated in detail in [30] that the SIA manifests superior retrieval accuracy to the Jacobian approach with a slight increase in computational costs. For this reason, the SIA is chosen for this work.

The ambiguity problem (also mentioned in Section 2.1.1) is a noted issue encountered in the retrieving stage [48], which occurs when mapping σ^0 from delay-Doppler to spatial domains. In other words, each DD cell is associated with two separate spatial clusters. Thus, it is hard to distinguish $\sigma^0(\vec{\rho}_a)$ and $\sigma^0(\vec{\rho}_b)$ individually ($\vec{\rho}_a$ and $\vec{\rho}_b$ denote two spatial clusters that correspond to the same DD cell) based on a single DDM. A feasible solution to this problem is proposed in [48], i.e., the dual antennas method. Implied by its name, two receiving antennas are utilized and the beams are tilted away from the ambiguity-free line. With two different beams (with which separate DDMs can be generated accordingly), the ambiguity problem in σ^0 retrieval can thus be fixed [31, 48].

In summary, the SIA and the dual antennas method are adopted in the σ^0 retrieval stage. Details related to these two methods for σ^0 retrieval can be found in [30].

3.1.2 WS Recovery

The Cox and Munk model [43] substantiates an empirical relationship between U_{10} and the sea surface mean square slope. Meanwhile, the sea surface scattering coefficient σ^0 is determined by MSS [39]. On the whole, with the knowledge of U_{10} over sea surface, the corresponding σ^0 can be determined and vice versa.

It should be noted that the Cox and Munk model [43] was initially proposed based on visible lights. In order to employ this model in the GNSS-R area, Katzberg *et al.* [44] developed an empirical calibration on this model to adjust to GNSS (L-band) signals, and the modified model is applied in this work. Furthermore, the feasibility of the Cox and Munk model for σ^0 simulation of tsunami-dominated sea surface has been verified in Section 2.3. For additional information on WS recovery from σ^0 distribution refer to [16, 34, 35].

With the above discussions in mind, the WS can readily be restored from the σ^0 distribution. In this work, the factor of wind direction is not considered and the value is set at $0°$ (with respect to the x-axis) for convenience (more information about retrievals of both WS and wind direction from DDMs can be found in [18]).

3.1.3 SSHA Determination

The Godin model [6] summarizes that for a tsunami-dominated sea surface, the effective wind speed is dependent on the tsunami parameters, and is distinguished from the background wind speed (WS_0 that is without tsunami) by a factor of M (see more details in Section 2.2).

Based on equations (2.9) and (2.10), tsunami-induced SSHA a can be determined

from the restored effective wind speed WS_{eff} together with the pre-known background wind speed WS_0 distribution and H, as well as associated tsunami parameters (T_0 and c) as

$$a = (1 - \frac{WS_{eff}}{WS_0})\frac{Hu_* \ln \beta}{\kappa c}.$$ (3.1)

It should be noted that c can be derived with given D, while in this chapter D is assumed as unknown. In order to obtain a, typical empirical values of T_0 and c can be first assigned as initial guesses and regarded as inputs to (3.1). With a closer look, it can be found that the term β that contains T_0 is on the order of 10^6 which is insensitive to the bias caused by T_0, so is $\ln \beta$. Furthermore, the pre-assigned c merely induces an overall bias in SSHA amplitude to a limited extent (usually less than 10%). With these in mind, it is believed that biases in SSHAs caused by initially assigned T_0 and c are insignificant, and tsunami parameters (e.g., c and T_0) to be estimated from these SSHAs will be almost immune to such biases. Thus, the updated c and T_0 are expected to be more closely aligned with true tsunami parameters. Because of this, it is more reasonable to refine SSHA, T_0 and c results through repeating SSHA determination and parameter estimation procedures with updated T_0 and c [49]. Moreover, this iteration process will be repeated until a convergence between the updated and the input T_0 and c is obtained where the biases between updated T_0 and c and the corresponding inputs are less than 1%. In case of failure in reporting tsunamis, SSHAs determined during the iteration period will not be inspected by the tsunami judging criteria (proposed in Section 3.2), while directly utilized for tsunami parameter estimations (investigated in Section 3.3). It is also worth mentioning that when the number of iterations is beyond five, the updates and

inputs are thus considered not consistent and the associated SSHA will be discarded.

3.2   Tsunami Detection

In order to determine the tsunami-induced SSHAs through the processes stated in Section 3.1.3, it must be assumed that the DDMs are of tsunami-dominated sea surfaces. Without this premise, the tsunami-induced wind perturbation model cannot be applied, however, this assumption may not hold true for most real-world scenarios. In reality, the sea surface does not always contain a tsunami while in this method all DDMs are assumed of tsunami-dominated sea surfaces. Therefore, the determined SSHAs must be accurately assessed to reduce false alarms. In this section, a tsunami detection precept is proposed and the associated criteria are detailed.

A monochromatic tsunami wave can be regarded as a sinusoidal wave [38]. Coincidentally, it has been reported in [46] that the leading wave of the 2004 Sumatra-Andaman tsunami measured by Jason-1 (over the range from (5.00°S, 83.96°E) to (1.00°N, 86.12°E)) can be well fitted to a sine wave with a wavelength of 580 km and an amplitude of 60 cm (see Figure 2.4(c)). Hence, with the presence of monochromatic tsunami waves the SSHAs should primarily follow the form of a sine wave. This is the first piece of judging criteria, namely a good fit to a sine wave.

Furthermore, tsunami waves in deep seas usually have a very long wavelength of several hundred kilometres and an amplitude of 20 to 100 cm [50]. These two combined characteristics distinguish tsunami waves from other ocean waves (e.g., tide waves and wind-generated waves) [51]. Therefore, fitting parameters (amplitude and wavelength) determined from the aforehand-noted fitting process act as the second

standard. To sum up, in the tsunami detection precept only those SSHAs sharing the characteristics of tsunami waves will be regarded as tsunami-induced.
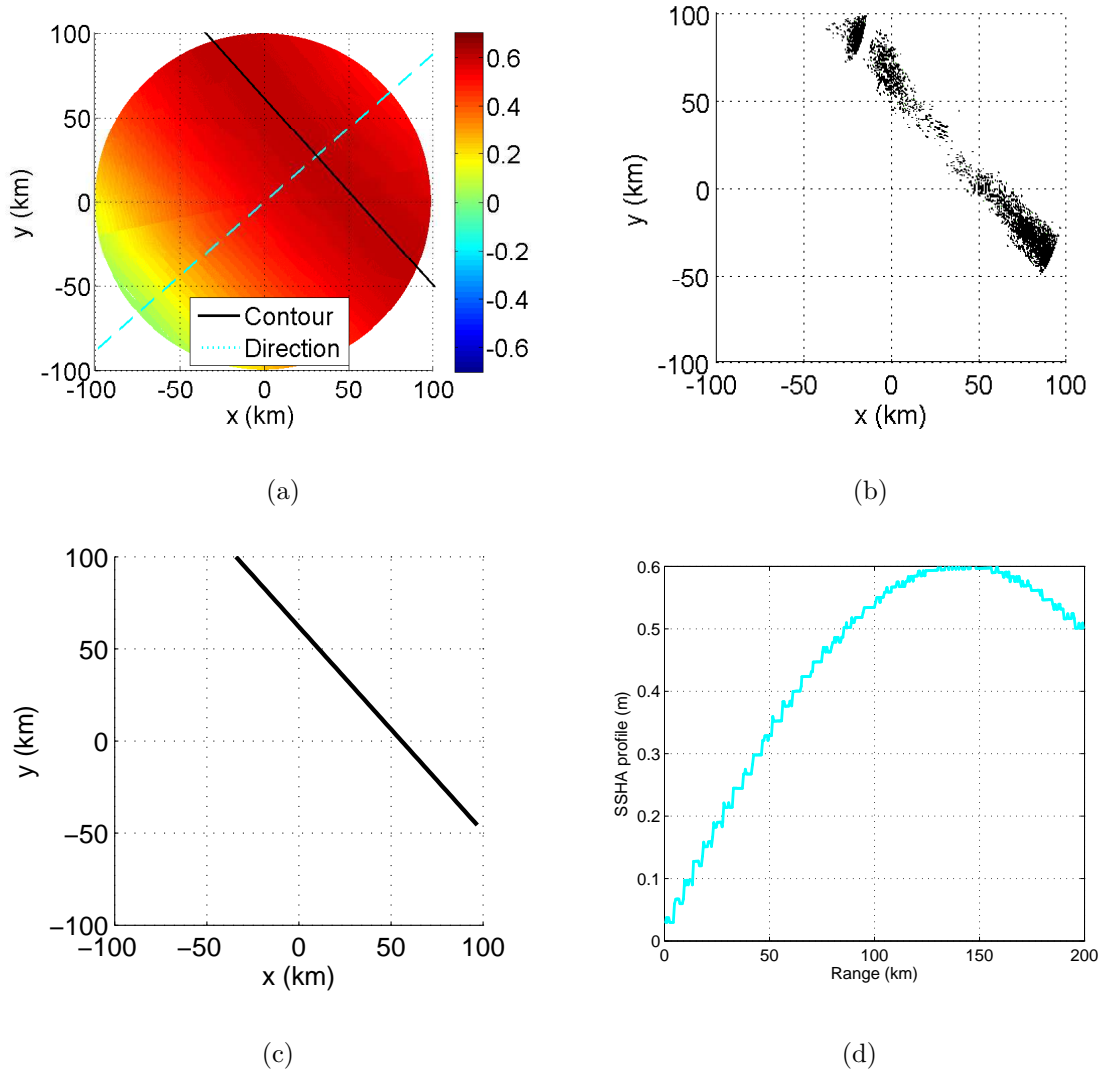

(a)

(b)

(c)

(d)

Figure 3.1: Illustration of SSHA profile extracting steps: (a) SSHA map with determined contour and propagation direction, (b) SSHA points around the peak value, (c) fitted contour and (d) extracted SSHA profile.

In application, a contour with the peak value of each derived SSHA map is to be

determined first. For illustration purposes, with an SSHA map (see Figure 3.1(a)) SSHA values falling within a certain scope (e.g., [peak value - 1, peak value] cm), are recorded and displayed in Figure 3.1(b). The contour can be obtained by fitting such points to a line as presented in Figure 3.1(c), and it is believed to be representative of the tsunami wave front. Accordingly, the direction perpendicular to this contour is regarded as the tsunami propagation direction. The 180° ambiguity in direction can be eliminated from visual inspection of SSHA results with a finer observation interval. The final resultant is shown as Figure 3.1(a) with determined contour (represented by the black solid line) and propagation direction (indicated by the cyan dash line). In order to reduce the computational cost for the fitting process, the SSHA profile is extracted from each SSHA map by passing through the SP in the estimated tsunami propagation direction. The corresponding SSHA profile extracted from Figure 3.1(a) is demonstrated in Figure 3.1(d). The range in Figure 3.1(d) is the distance from each point on the cyan dash line (within the glistening zone) to the left-bottom intersection of the cyan dash line and the outer boundary of the glistening zone in Figure 3.1(a). In addition, successive zeros in SSHA profiles must be rejected, otherwise the subsequent sine wave-based fitting process will be adversely affected.

With the extracted SSHA profile, the fitting process can be executed, and the sine wave model is applied as

$$\text{SSHA}(r) = A\sin(kr + \phi), \tag{3.2}$$

where A, k, and ϕ are tsunami SSHA amplitude, non-directional wave number and phase shift, and r is the range variable. Furthermore, with the fitting coefficients determined, the corresponding tsunami-wave parameters can also be interpreted.

44

Briefly, tsunami amplitude A can be determined directly and the tsunami wavelength (λ) can be calculated by $\lambda = 2\pi/k$. More details of tsunami parameter estimation are addressed in Section 3.3.

As previously stated, the tsunami detection scheme relies on the geometrical similarity between the derived SSHA and a real tsunami wave, which can be modelled by a sinusoid with a wavelength of hundreds of km and an amplitude of 20 to 100 cm. For that reason, the tsunami detection precept is specified as the following criteria [49]:

- Good fit to a sine wave with a root mean square error (RMSE) of less than 0.01;

- Sufficient tsunami amplitude with an SSHA amplitude (A) greater than 20 cm;

- Long wavelength with a λ no less than 100 km (or equivalently, $k \leq 6.3 \times 10^{-5}$ rad/m).

It should be noted that in reality the threshold of RMSE may become higher than 0.01. The input SSHA in this work is an ideal sine wave and the corresponding retrieval results manifest high accuracy, therefore a good fit to the sine wave has been obtained. Nevertheless, a real-world tsunami wave may not strictly follow the form of a sinusoidal wave and the goodness of fit may recede accordingly. Furthermore, the retrieval performance will degrade from measured DDMs. Despite this, A and λ (or k) meet those requirements listed above so that the SSHA profile may be detected as a tsunami wave.
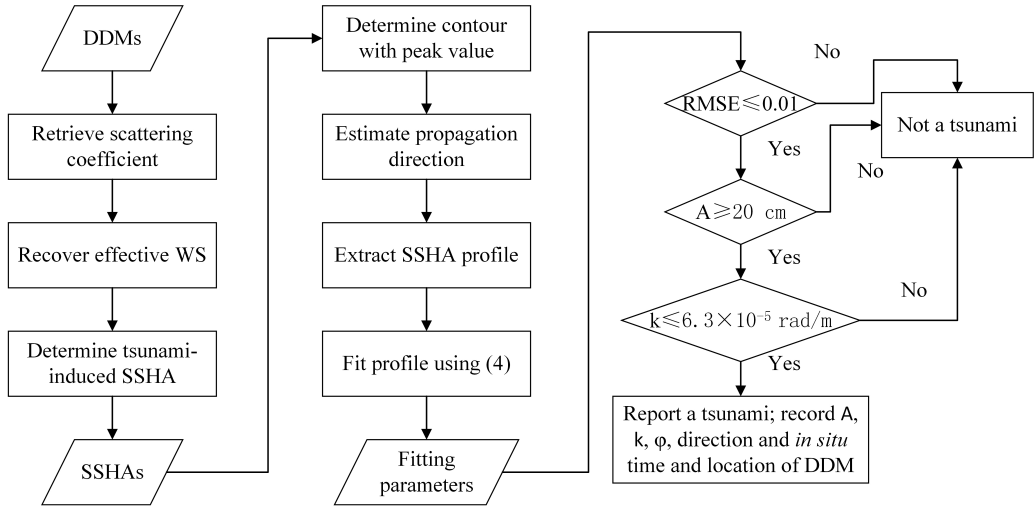
Figure 3.2: Flowchart of tsunami-induced SSHA determination and tsunami detection.

3.3 Tsunami Parameter Estimation

In Section 3.1 and Section 3.2, determination of SSHAs from DDMs as well as a tsunami detection precept has been investigated and the corresponding process flowchart is displayed in Figure 3.2.

After the tsunami detection procedure, the SSHA results/profiles judged as truly tsunami-induced are retained for further tsunami parameter estimation. In fact, certain tsunami parameters (i.e., the tsunami wave amplitude, propagation direction, and wavelength) have already been determined during the former detecting operation.

Based on the previous analysis, the tsunami source location is believed to be on the cyan dash line (tsunami propagation direction) in Figure 3.1(a). Similarly, with an additional allopatric measurement another line that passes through the new SP in the corresponding estimated propagation direction can also be determined and the intersection of two such lines is regarded as the tsunami source location.

46

In order to investigate the tsunami propagation velocity estimation, two approaches are proposed as follows.

3.3.1 Fitting-based Estimation Method

The fitting-based tsunami propagation velocity estimation method (hereafter, the fitting-based method) mainly depends on the fitted phase shift ϕ.

The tsunami propagation velocity can be deduced from the phase shift difference $\Delta\phi$ between each fitted SSHA profile at separate time intervals, i.e.,

$$c = \frac{\Delta\phi_{mn}}{k\Delta t_{mn}}, \tag{3.3}$$

where $\Delta\phi_{mn}$ and Δt_{mn} denote the phase shift and time differences between mth and nth fitted SSHA profiles of confirmed tsunami waves.

3.3.2 Tracking-based Estimation Method

The tracking-based method is an alternative method proposed for tsunami propagation velocity estimation. This method may be more preferable in real-world applications. The procedure is introduced as follows. After the detection process, a new contour of 20 cm (the threshold of SSHA amplitude for tsunami detection) is determined from the whole SSHA map (the contour with peak value was previously utilized). By tracking the contour of 20 cm at different moments, the tsunami propagation velocity can be deduced.

3.4 Results

The December 26, 2004 Sumatra-Andaman tsunami is also used as an example to test the above-mentioned tsunami-induced SSHA determination, tsunami detection precept and parameter estimation.

3.4.1 Tsunami-induced SSHA

In order to display a full passage of a tsunami wave over the region under surveillance (centred around (6.01° S, 83.60° E)) with limited figures, an interval of 10 min between each adjacent simulated DDM is chosen for this work. It should be note that tsunami can be detected based upon confirmed tsunami-induced SSHAs regardless of the detection interval. Details of simulating DDMs of tsunami-dominated sea surfaces are addressed in Chapter 2. The GNSS-R simulation parameters and dual-antenna features are in accordance with those in [31] and shown in Table 3.1.

Figure 3.3 illustrates σ^0 retrieval results using the dual antennas-based SIA method. Figure 3.3(a) represents the σ^0 retrieved from a DDM that is collocated with background WS_0 measurement and is regarded as the initial observation. The time gaps between the initial detection in Figure 3.3(a) and those from Figure 3.3(b) to Figure 3.3(f) are: 10 min, 20 min, 30 min, 40 min and 50 min, respectively.

Figure 3.4 shows the corresponding recovered WS resulting from Figure 3.3.

Both σ^0 retrieval in Figure 3.3 and WS restoration in Figure 3.4 demonstrate high accuracy during the retrieving/restoring stage. Good retrieval performance lays a solid foundation for later SSHA determination and ultimately for tsunami detection and parameter estimation.
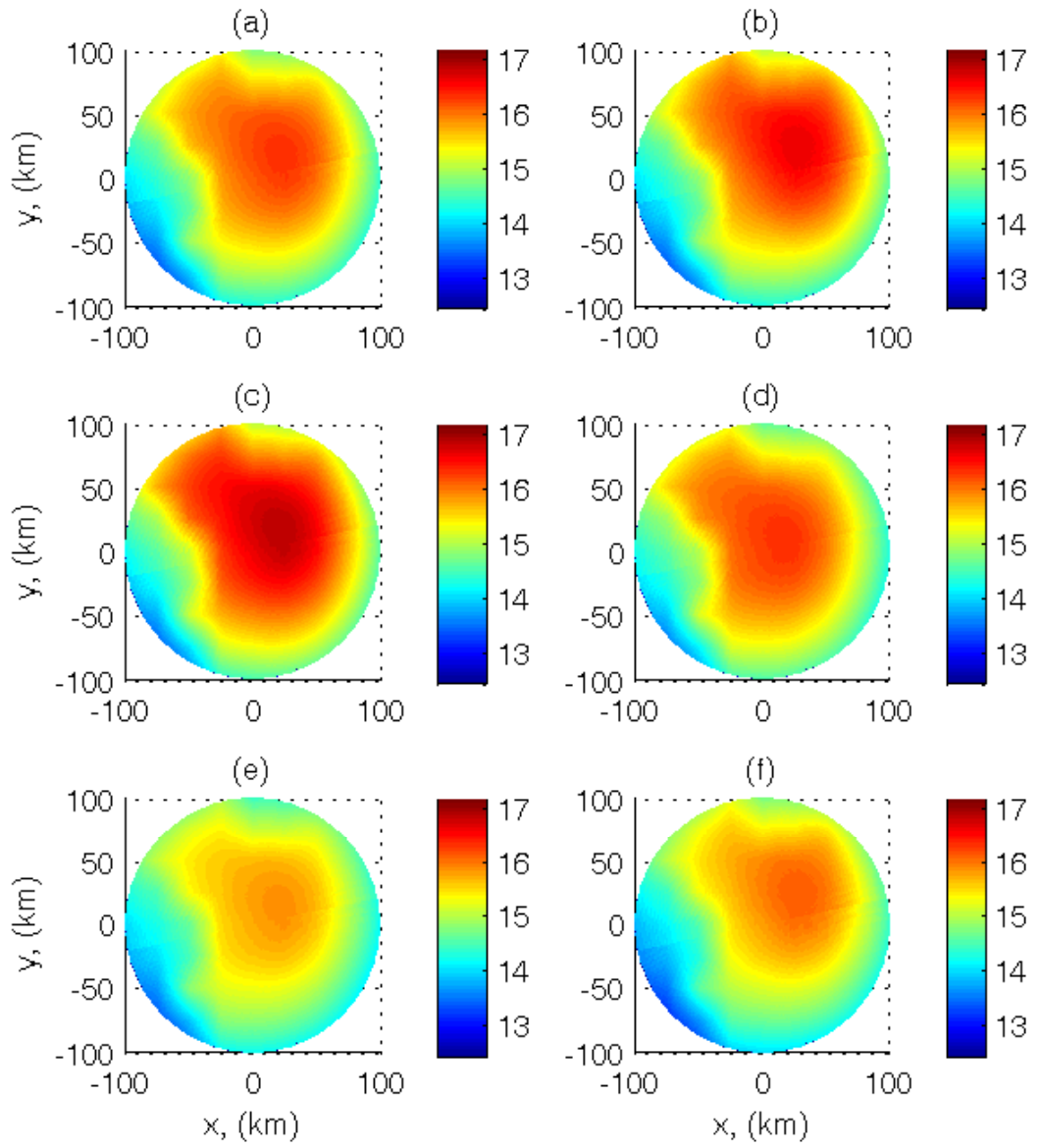
Figure 3.3: σ^0 retrieval using the dual antennas-based SIA method from DDMs of: (a) initial observation, and (b) 10 min, (c) 20 min, (d) 30 min, (e) 40 min, and (f) 50 min after the initial observation.
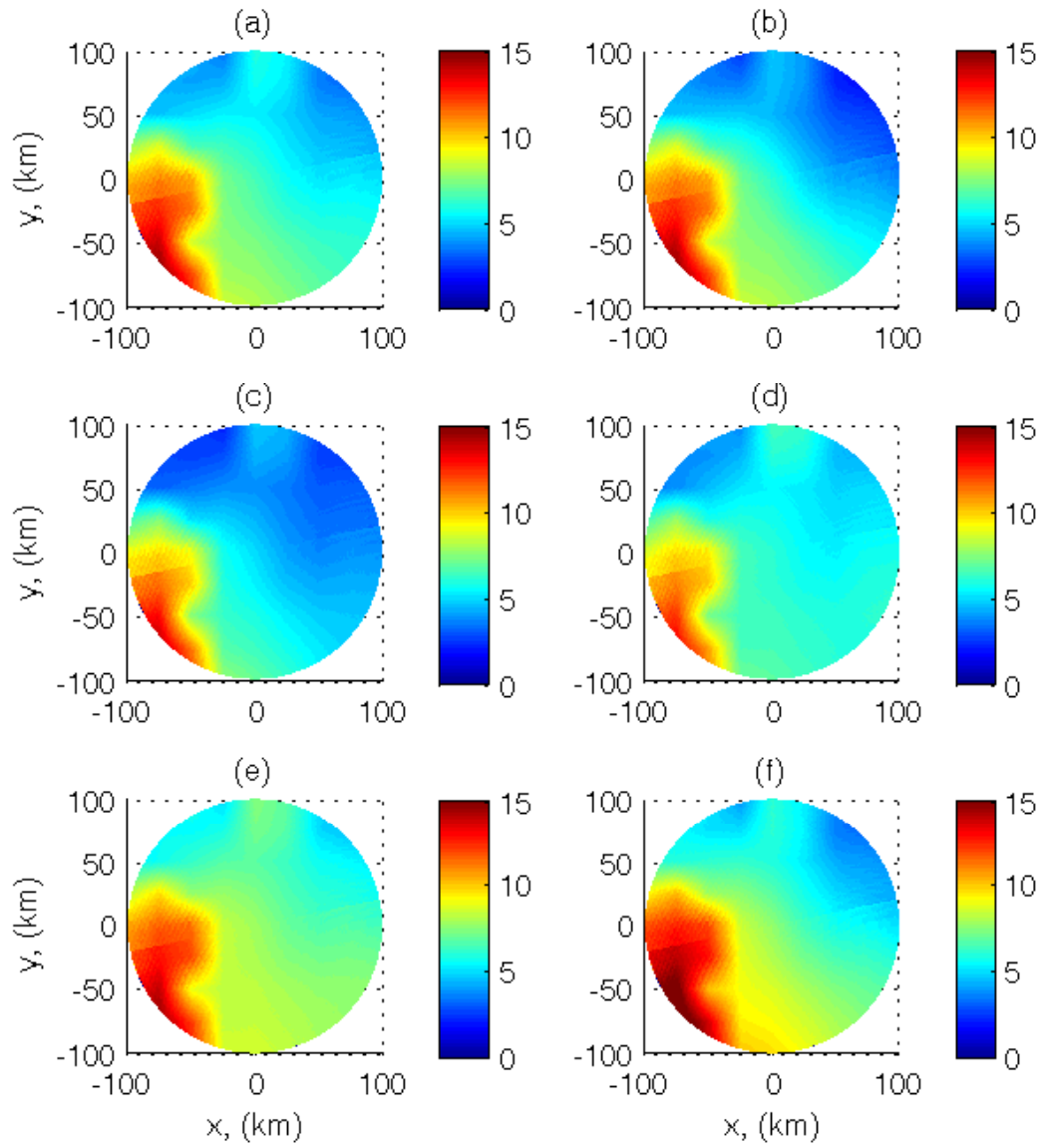
Figure 3.4: Corresponding WS restoration resulting from retrieved σ^0 in Figure 3.3.

Table 3.1: DDM Simulation Scenario

Simulation parameters	Value/unit
Transmitter height	20000 km
Receiver height	680 km
Grazing angle at SP	76°
Antenna 1 tilting angle	-9°
Antenna 2 tilting angle	12°
Transmitter velocity	(-2.72, 2.68, -0.65) km/s
Receiver velocity	(7.21, 1.23, 1.72) km/s
SP position	(6.01° S, 83.60° E)

With recovered WS_{eff}, SSHAs can be determined using (3.1). In reality, H can be measured by a tethersonde system [52]. Due to a lack of collocated tethersonde data, the typical empirical value is employed as $H = 60$ m [6]. In addition, the measurement of QuikSCAT on its orbit 28744 is chosen as WS_0. It should be noted that the proposed method requires a background WS_0, which is preferred to be obtained immediately before the tsunami. Although QuikSCAT data are used as the background wind speeds here, the retrieved wind speed from GNSS data without tsunami instead of measurements from an ancillary instrument can be employed. As demonstrated in Section 3.1.3, typical values $T_0 = 40$ min and $c = 200$ m/s [6] are to be assigned as initial inputs and will be updated in accordance with the tsunami wave that is under investigation after the iteration process. In particular, in order to illustrate the convergence performance of the iteration process the input value of c is designedly

distinguished from 200 m/s (true value is 201.42 m/s) and is set as 150 m/s. Using the retrieved WS_{eff} results in Figure 3.4 and the above-noted parameters, the iteration is processed and the results are listed in Table 3.2. From Table 3.2, it can be seen that the desirable results of T_0 and c are obtained with two iterations. The updated T_0 and c results can then be taken as reliable inputs. Verified by comprehensive simulation results, it has been found that after one or two iterations, T_0 and c can be accurately determined from true tsunami waves irrespective of acceptable biases in initial guesses, and therefore, so can the SSHA.

Table 3.2: Iteration Outputs

	c (m/s)	T_0 (s)
True value	201.42	2900.00
Initial guesses	150.00	2400.00
1st iteration	203.64	2909.92
2nd iteration	203.62	2892.26

All things considered, the tsunami-induced SSHAs are to be determined from GNSS-R DDMs for the first time. Figure 3.5 presents the SSHAs derived from Figure 3.4 based on updated T_0 and c. In Figure 3.5(a), the SSHA is determined from the initial observation, which is supposed to be zero-distributed (according to (3.1)). Nonetheless, some errors can be observed and they are believed to be introduced during the retrieving steps investigated in Section 3.1. Such errors also exist in subsequent observations. For this reason, Figure 3.5(a) is regarded as an error map

caused by the overall derivation process and is subtracted from each sub-plot in Figure 3.5 to mitigate such errors. A better accuracy has been achieved after error reduction manipulation. Consequently, the corresponding SSHA maps are shown in Figure 3.6 and the updated results are retained for further investigations (tsunami detection procedure and parameter estimation). From an intuitive inspection of Figure 3.5 or Figure 3.6, the passage of tsunami waves over this region is distinct. For reference, the input SSHA follows the form of a sine wave with a wavelength of 580 km and an amplitude of 60 cm. The manifestations of SSHAs as sine waves will be illustrated after the extraction of SSHA profiles, and the parameters can also be estimated.

3.4.2 Tsunami Detection Outcome

By employing the tsunami detection precept proposed in Section 3.2, the detection procedure can be performed on the extracted SSHA profiles. Only the SSHA profile confirmed to those three judging criteria simultaneously will be reported as a tsunami. Moreover, the SSHA associated with the initial observation (contains no tsunami) is zero after error reducing and will be invalid after the zero-removal process. Because of this, an additional observation at the 60 min-interval after the initial observation is made for the tsunami detection test. The SSHA profiles extracted from the new observation and Figures 3.6(b)–(f) are then inspected by this detection precept and they are all detected as tsunami waves. The detection outcomes are summarized in Table 3.3. The corresponding SSHA profiles along with each fitting curve are shown in Figure 3.7. As mentioned at the end of Section 3.4.1, it has been illustrated that the SSHA profiles follow the form of sine waves.
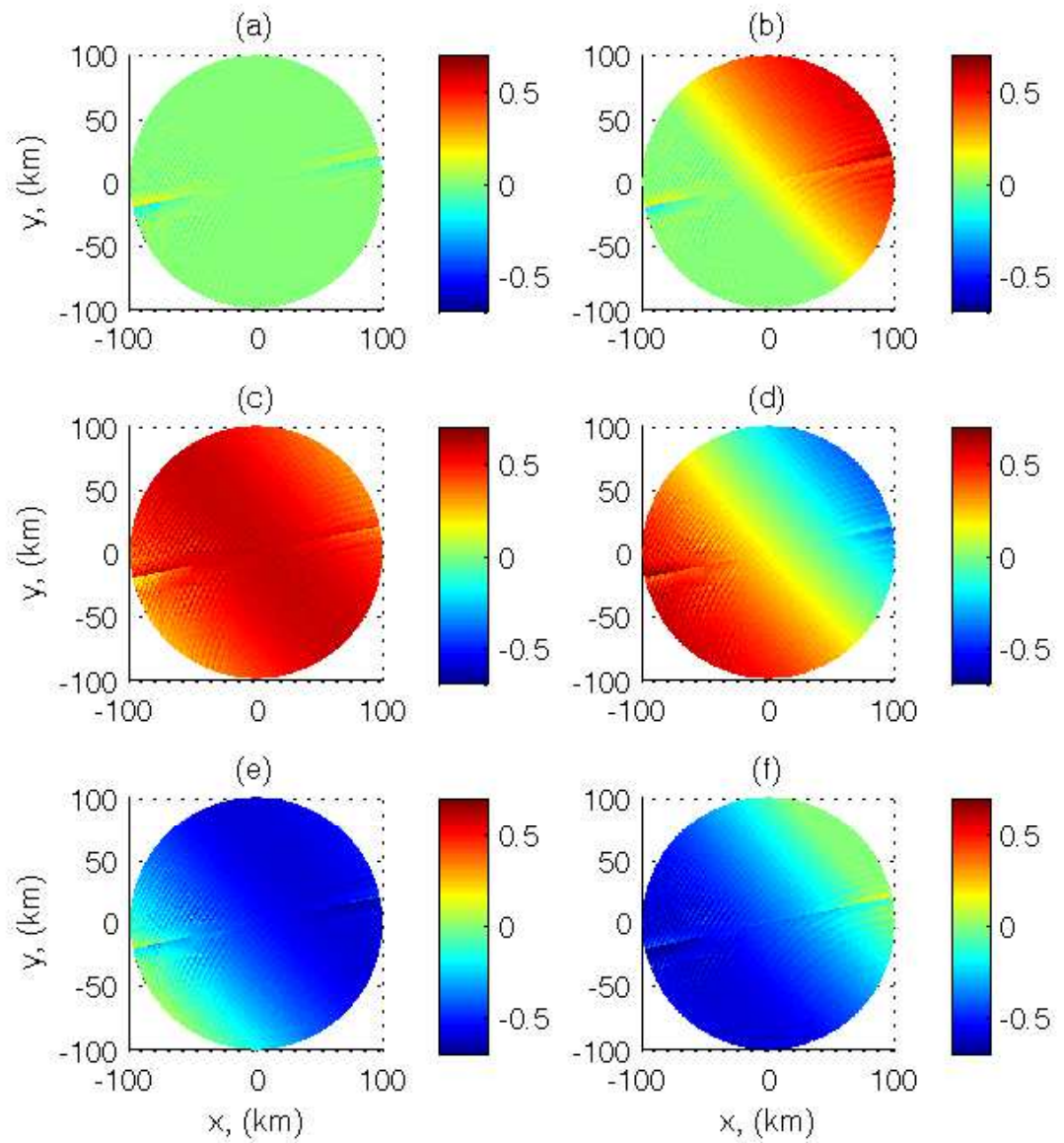
Figure 3.5: SSHA retrievals during a tsunami passage. (a) No tsunami; and with: (b) a margin of tsunami leading front, (c) the tsunami crest, (d) transition part between the crest and trough, (e) the tsunami trough, and (f) the tail of tsunami leading front.
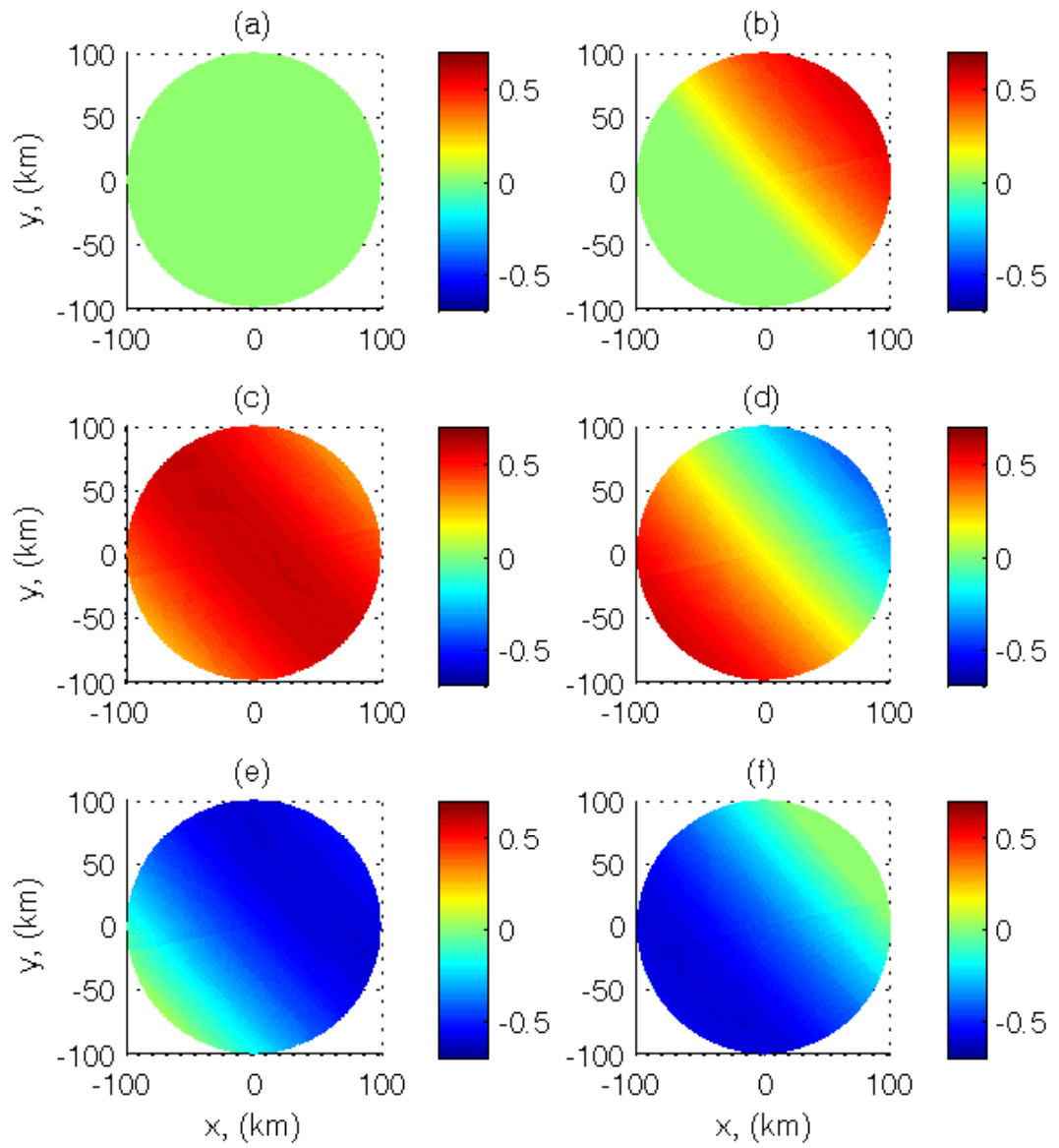
Figure 3.6: Error-reduced results originated from Figure 3.5. Subplot (a) results from the initial observation and each time gap between subplot (a) is: (b) 10 min, (c) 20 min, (d) 30 min, (e) 40 min, and (f) 50 min.
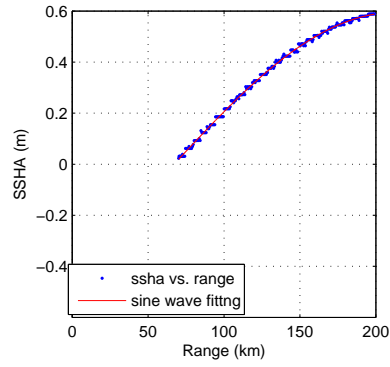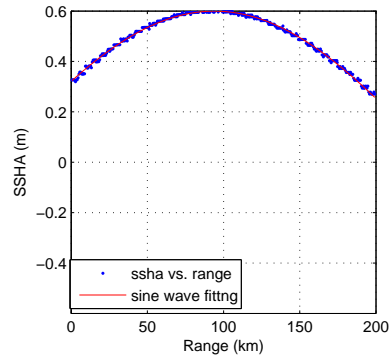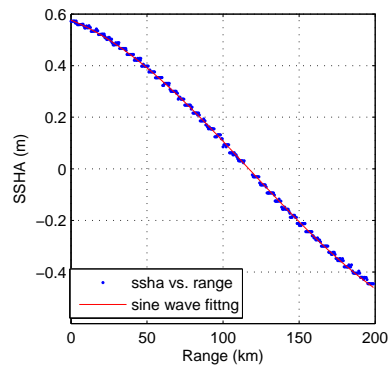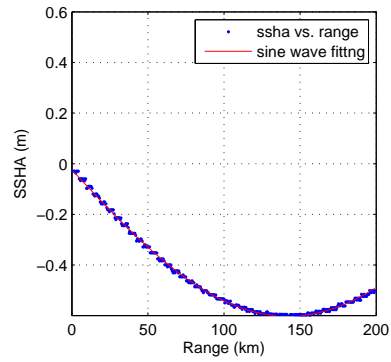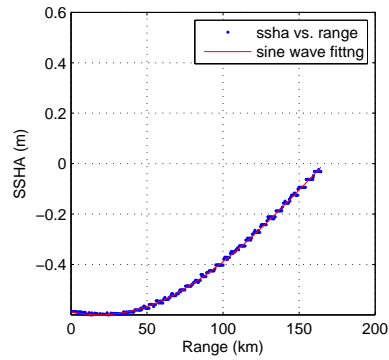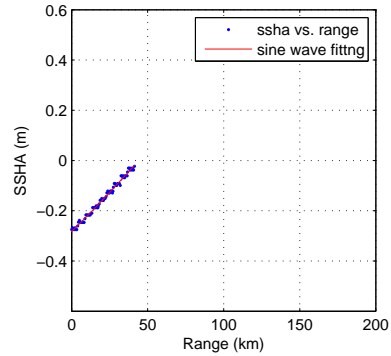
Figure 3.7: Detected tsunami waves by fitting process with time gaps to the initial observation: (a) 10 min, (b) 20 min, (c) 30 min, (d) 40 min, (e) 50 min, and (f) 60 min.

Table 3.3: Detection Outcome

Time gap to initial observation (min)	10	20	30	40	50	60
RMSE ≤ 0.01	√	√	√	√	√	√
Tsunami amplitude $A \geq 20$ (cm)	√	√	√	√	√	√
Wavelength $\lambda \geq 100$ (km)	√	√	√	√	√	√
Tsunami detected	√	√	√	√	√	√

The estimated tsunami parameters based on the fitted sine waves in Figure 3.7 have been tabulated in Table 3.4. The averaged estimates of tsunami wave amplitude, propagation direction and wavelength are 60.03 cm, 222.76° and 585.82 km.

Table 3.4: Tsunami Parameters Estimation

Time gap to initial observation (min)	10	20	30	40	50	60	input
Tsunami amplitude (cm)	59.51	59.96	61.96	60.29	59.98	58.46	60.00
Propagation direction (deg)	224.71	223.16	221.55	222.00	221.84	223.33	221.60
Wavelength (km)	586.63	586.83	615.50	583.09	591.98	550.91	580.00

When it comes to propagation direction estimation, all steps summarized in Figure

57

3.2 are implemented for a new region with the SP around (1.01°S, 85.39°E) and the estimated tsunami propagation direction of 207.22°. The corresponding estimated direction is 222.76° at (6.01°S, 83.60°E). Thus, the tsunami source location can be estimated as (3.18°N, 93.53°E). For reference, the input is (3.40°N, 94.20°E).

In addition, the fitting-based tsunami propagation velocity estimations are listed in Table 3.5 using the fitted phase shifts obtained based on Figure 3.7. The mean velocity is computed as 202.87 m/s and the input is 201.42 m/s. As a high velocity is obtained, which is intrinsic to a deep-sea tsunami [38], the presence of a tsunami is further confirmed.

Table 3.5: Fitting-based Tsunami Propagation Velocity Estimation

Time gap to initial observation (s)	600	1200	1800	2400	3000	3600
Fitted phase shift ϕ (rad)	0.59	1.89	3.20	4.48	5.82	7.09
Phase shift difference $\Delta\phi$ (rad)		1.30	1.31	1.28	1.34	1.27
Wavenumber k (10^{-5} rad/m)		1.08	1.07	1.06	1.07	1.06
Velocity estimation (m/s)		200.61	204.05	201.26	208.72	199.69

In order for the tracking-based method to work properly, observations with fine time intervals were required and the corresponding simulations with a 4-min gap were conducted for illustration purposes. Based on that, the traces of 20-cm contours with a gap of 4 min are displayed in Figure 3.8. The lines in different formats represent the positions of the contour at different times. From the upper-right corner to the

bottom-left corner, the 20-cm contours are obtained at 4 min, 8 min, 12 min, and 16 min after the initial observation. By calculating the distance from each contour to the point of (-100, -100), the distance difference between each contour can be derived, and the velocity is then to be estimated accordingly. The estimates of velocity are shown in Table 3.6 with a mean value of 203.83 m/s.
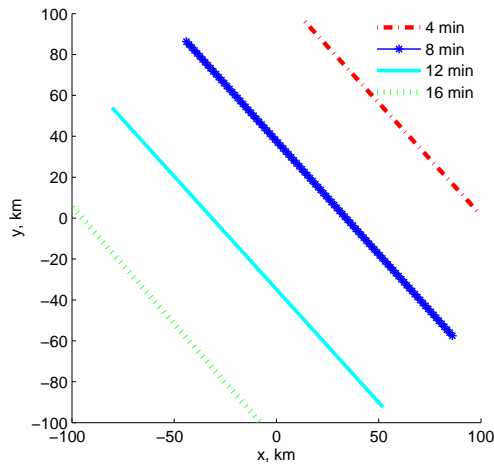
Figure 3.8: 20-cm contour locations after every 4 min. The arrow illustrates the tsunami propagation direction.

Table 3.6: Tracking-based Tsunami Propagation Velocity Estimation

Time gap between initial observation (min)	4	8	12	16
Distance to (-100,-100) (km)	216.19	166.50	117.86	69.43
Distance difference (km)		49.69	48.64	48.43
Tsunami propagation velocity (m/s)		207.04	202.67	201.79

3.4.3 Fitting- v.s. Tracking-based Methods

In summary, the phase shift changes over time are used in the fitting-based method. The tracking-based method employs the wave contour of fixed value over time.

For comparison purposes, the velocity estimated through the fitting-based method using the same 4 min-gap SSHA results is calculated as 209.69 m/s. For the fitting-based method, the estimation significantly depends on the ratio between fitted phase shift difference $\Delta\phi$ and wavenumber k ($\Delta\phi_{mn}/k$). It should be noted that k is on the order of 10^{-5} rad/m, which means a tiny error in $\Delta\phi$ will lead to a huge bias in the final result. Moreover, real-world estimates of $\Delta\phi$ may be less reliable and the result would be even worse. Nevertheless, the tsunami wave amplitude can roughly remain constant during the propagation in deep seas because of an insignificant energy loss [51]. Hence, the tracking-based method is believed to provide more accurate and reliable estimation on tsunami propagation velocity in real practices.

3.5 General Chapter Summary

This chapter presents a scheme of tsunami detection and parameter estimation from GNSS-R DDMs. The sea surface scattering coefficients are first retrieved from DDMs using the dual antennas-based SIA method. Afterwards, the sea surface wind speed distribution is recovered based on the scattering coefficient retrieval. The primary contribution of this paper is to determine tsunami-induced SSHAs from restored WS distribution by assuming all DDMs are of tsunami-dominated ocean surfaces. In addition, the SSHA distribution resulting from the tsunami-free DDM (which is supposed to be zero) is considered as an error map introduced during the overall retrieving

stage and is utilized to mitigate such errors from influencing subsequent SSHA results. Moreover, this chapter proposes a precept to judge the SSHA results and detect tsunamis, thereby reducing the false alarm rate. Last but not least, tsunami parameters are, for the first time, estimated from GNSS-R DDMs. The accuracy and feasibility of this scheme have been verified through comprehensive simulation tests on the 2004 Sumatra-Andaman tsunami event.

Chapter 4

Conclusion

4.1 Summary of Significant Results

In this thesis, research for improving tsunami remote sensing using the Global Naviga-
tion Satellite System-Reflectometry delay-Doppler maps has been presented. Firstly,
a detailed process to simulate the DDM of a tsunami-dominant sea surface is proposed.
Secondly, a DDM-based scheme for tsunami detection and parameter estimation is
developed.

The DDM simulation of tsunami-dominated sea surface is based on the Zavorotny
and Voronovich (Z-V) bistatic scattering model [41], the Cox and Munk sea sur-
face mean square slope model [43] and the tsunami-induced wind speed perturbation
model [6]. By combining the first two models, capability of DDMs in tsunami-free
ocean surface wind sensing has already been investigated [16–18]. In order to achieve
DDMs of a tsunami scenario, the wind speed during a tsunami event is modeled us-
ing the widely accepted tsunami-induced wind speed perturbation model. Followed

by the introduction to this simulation process, the feasibility of the Cox and Munk model [43] under a tsunami scenario is examined by comparing the simulated scattering coefficient with the Jason-1 measurement. After verifying the applicability, the tsunami DDM simulation can be accomplished through inputting the background wind speed over the sea surface and the tsunami-induced sea surface height anomalies. Afterwards, the simulation results before and during a tsunami over a region of interest are presented. Through analysis, the passage of the tsunami over this region can be interpreted based on the observation of tsunami-induced variations in scattering coefficient and DDMs. Hence, the possibility of detecting tsunamis from DDMs is illustrated according to the simulation results. This simulation work provides a foundation for the GNSS-R DDM-based tsunami detection and parameter estimation.

A further investigation is then carried out to fully reveal the capability of GNSS-R DDMs in tsunami detection and parameter estimation. Based on sea surface roughness being disturbed by the presence of a tsunami (which is due to the tsunami-induced sea surface wind speed perturbation [6, 38]), tsunami-induced variations in sea surface scattering coefficients and DDMs are employed for detecting tsunamis [35]. By applying the dual antennas-based SIA approach, the Cox and Munk model, and the tsunami-induced wind perturbation model, the tsunami-induced SSHAs are, for the first time, determined from GNSS-R DDMs. For robustness, a tsunami detection precept is also conceived and the SSHAs are judged based on the presence or absence of a tsunami. This procedure is especially important since accuracy and reliability are the key points in tsunami detection and early warning. Subsequently, tsunami parameters (wave amplitude, propagation direction and speed, wavelength,

and source location) are estimated on the account of the tsunami-induced SSHAs. The tsunami detection precept and parameter estimation have been tested with simulated data based on the 2004 Sumatra-Andaman tsunami event. The errors of estimated tsunami wave amplitude, propagation direction and velocity, wavelength and source location are 0.03 cm, 1.16°, 1.45 m/s, 5.82 km and (-0.22°N, -0.67°E), respectively.

4.2 Suggestions for Future Work

In general, the research has demonstrated the capability of GNSS-R DDM in deep-ocean tsunami detection. A problem during the retrieval process from GNSS-R DDM is the occurrence of errors around the ambiguity-free line, which can be clearly noted in Figure 3.5. After an error-reducing step, errors have been significantly reduced but still exist (see Figure 3.6). If the tsunami propagation direction coincides with the ambiguity-free line, the values of extracted SSHA profiles will be adversely influenced. Therefore, a further improvement on error elimination will positively contribute to this work. Furthermore, in order to manifest a full passage of the tsunami wave over a fixed region, the GNSS-R is assumed to be able to observe the same area continuously by assuming the transmitter and the receiver are fixed over time in present work. In a real scenario, the error map may not be directly utilized since the change in the GNSS-R geometry will lead to a change in the orientation of the ambiguity-free line. However, rotating the simulated error map according to actual GNSS-R geometry variation may be one possible solution to this problem. In the future, it may be interesting to repeat the work for moving platforms using different tracks with respect to the tsunami propagation direction. Moreover, it is worth

mentioning that the thresholds set for the fitting process may be adjusted for real-world applications, in which tsunami-induced SSHAs are not perfectly in accord with sine waves. It is necessary to further verify the proposed tsunami-dominated sea surface DDM simulation method using collected GNSS-R data and corresponding measured background and effective wind speed datasets during a tsunami event. It is also necessary to further validate the proposed tsunami detection and parameter estimation scheme using measured GNSS-R data and collocated *in situ* wind speed and tsunami wave amplitude datasets in the future. However, this study is not possible today as the available data for this research is limited. This may become possible with the launch of new spaceborne GNSS-R missions, e.g., TechDemoSat-1 and Cyclone GNSS (CYGNSS) [53].

Bibliography

[1] J. Clague, A. Munro, and T. Murty, "Tsunami hazard and risk in Canada," *Nat. Hazards*, vol. 28, nos. 2-3, pp. 433-461, 2003.

[2] R. Cochard, S. L. Ranamukhaarachchi, G. P. Shivakoti, O. V. Shipin, P. J. Edwards, and K. T. Seeland, "The 2004 tsunami in Aceh and Southern Thailand: A review on coastal ecosystems, wave hazards and vulnerability," *Perspect. Plant Ecol. Evol. Systemat.*, vol. 10, no. 1, pp. 3-40, 2008.

[3] E. N. Bernard and C. Meinig, "History and future of deep-ocean tsunami measurements," in *Proc. OCEANS*, Kona, HI, USA, 2011.

[4] C. Falck, M. Ramatschi, M. Bartsch, and A. Merx, "The GNSS-based component of the German-Indonesian Tsunami Early Warning System (GITEWS): Overview, first operation results and current developments," in *Proc. IEEE Int. Geosci. Remote Sens. Symp.*, Honolulu, HI, USA, pp. 134-137, Jul. 2010.

[5] K. Yu, "Tsunami-wave parameter estimation using GNSS-based sea surface height measurement," *IEEE Trans. Geosci. Remote Sens.*, vol. 53, no. 5, pp. 2603-2611, May. 2015.

[6] O. A. Godin, V. G. Irisov, R. R. Leben, B. D. Hamlington, and G. A. Wick, "Variations in sea surface roughness induced by the 2004 Sumatra-Andaman tsunami," *Nat. Hazards Earth Syst. Sci.*, vol. 9, no. 4, pp. 1135-1147, Jul. 2009.

[7] B. D. Hamlington, R. R. Leben, O. A. Godin, and V. G. Irisov, "On the feasibility of tsunami detection using satellite-based sea surface roughness measurements," in *Proc. IEEE Int. Geosci. Remote Sens. Symp.*, Honolulu, HI, USA, pp. 3035-3038, Jul. 2010.

[8] D. Barrick, "A coastal radar system for tsunami warning," *Remote Sens. Environ.*, vol. 8, pp. 353-358, 1979.

[9] K. W. Gurgel, A. Dzvonkovskaya, T. Pohlmann, T. Schlick, and E. Gill, "Simulation and detection of tsunami signatures in ocean surface currents measured by HF radar," *Ocean Dyn.*, vol. 61, no. 10, pp. 1495-1507, Oct. 2011.

[10] C.-L. Mai and J.-F. Kiang, "Reconstruction of ionospheric perturbation induced by 2004 Sumatra tsunami using a computerized tomography technique," *IEEE Trans. Geosci. Remote Sens.*, vol. 47, no. 10, pp. 3303-3312, Oct. 2009.

[11] Y.-M. Yang, J. L. Garrison, and S.-C. Lee, "Wavelet filtering of gps network data for identification of ionospheric disturbances associated with tsunamis," in *Proc. IEEE Int. Geosci. Remote Sens. Symp.*, Honolulu, HI, USA, pp. 2956-2959, Jul. 2010.

[12] S. Jin, G. P. Feng, and S. Gleason, "Remote sensing using GNSS signals: Current status and future directions," *Adv. Space Res.*, vol. 47, no. 10, pp. 1645-1653, May. 2011.

[13] S. Gleason, "Remote sensing of ocean, ice and land surfaces using bistatically scattered GNSS signals from low earth orbit," PhD Thesis, University of Surrey, 2006.

[14] M. Martin-Neira, "A passive reflectometry and interferometry system (PARIS): Application to ocean altimetry," *ESA J.*, vol. 17, no. 4, pp. 331-355, 1993.

[15] J. L. Garrison, A. Komjathy, V. U. Zavorotny, and S. J. Katzberg, "Wind speed measurements using forward scattered GPS signals," *IEEE Trans. Geosci. Remote Sens.*, vol. 40, no. 1, pp. 50-65, Jan. 2002.

[16] M. Clarizia, C. Gommenginger, S. Gleason, M. Srokosz, C. Galdi, and M. Bisceglie, "Analysis of GNSS-R delay-Doppler maps from the UK-DMC satellite over the ocean," *IEEE Geosci. Remote Sens. Lett.*, vol. 36, no. 2, 2009.

[17] C. Li and W. Huang, "Sea surface wind retrieval from GNSS delay-Doppler map using two-dimension least-squares fitting," in *Proc. IEEE OCEANS*, Bergen, Norway, 2013.

[18] C. Li and W. Huang, "An algorithm for sea surface wind field retrieval from GNSS-R delay-Doppler map," *IEEE Geosci. Remote Sens. Lett.*, vol. 11, no. 12, pp. 2110-2114, Dec. 2014.

[19] A. Komjathy, J. Maslanik, V. U. Zavorotny, P. Axelrad, and S. J. Katzberg, "Sea ice remote sensing using surface reflected GPS signals," in *Proc. IEEE Int. Geosci. Remote Sens. Symp.*, Honolulu, HI, USA, pp. 2855-2857, Jul. 2000.

[20] S. Gleason, "Towards sea ice remote sensing with space detected GPS signals:

Demonstration of technical feasibility and initial consistency check using low resolution sea ice information," *Remote Sens.* vol. 2, no. 8, pp. 2017-2039, Aug. 2010.

[21] F. Fabra, E. Cardellach, O. Nogues-Correig, S. Oliveras, S. Ribo, A. Rius, M. Belmonte-Rivas, M. Semmling, G. Macelloni, S. Pettinato, R. Zasso, and S. D'Addio, "Monitoring sea-ice and dry snow with GNSS reflections," in *Proc. Int. Geosci. Remote Sens. Symp.*, pp. 3837-3840, Jul. 2010.

[22] K. M. Larson, E. D. Gutmann, V. U. Zavorotny, J. J. Braun M. W. Williams, and F. G. Nievinski, "Can we measure snow depth with GPS receivers," *Geophys. Res. Lett.*, vol. 36, no. 17, Sept. 2009.

[23] F. Fabra, E. Cardellach, O. Nogues-Correig, S. Oliveras, S. Ribo, A. Rius, G. Macelloni, S. Pettinato, and S. D'Addio, "An empirical approach towards characterization of dry snow layers using GNSS-R," in *Proc. Int. Geosci. Remote Sens. Symp.*, pp. 4379-4382, Jul. 2011.

[24] A. Egido, G. Ruffini, M. Caparrini, C. Martn, E. Farres, and X. Banque, "Soil moisture monitorization using GNSS reflected signals," in *Proc. 1st Colloq. Sci. Fundam. Aspects Galileo Programme*, Toulouse, France, pp. 1-4, Oct. 2007.

[25] N. Rodriguez-Alvarez, X. Bosch-Lluis, A. Camps, M. Vall-Ilossera, E. Valencia, J. F. Marchan-Hernandez, and I. Ramos-Perez, "Soil moisture retrieval using GNSS-R techniques: Experimental results over a bare soil field," *IEEE Trans. Geosci. Remote Sens.*, vol. 47, no. 11, pp. 3616-3624, Nov. 2009.

[26] R. Sabia, M. Caparrini, G. Ruffini, "Potential synergetic use of GNSS-R signals to improve the sea-state correction in the sea surface salinity estimation: Application to the SMOS mission," *IEEE Trans. Geosci. Remote Sens.*, vol. 45, no. 7, pp. 2088-2097, Jul. 2007.

[27] J. Marchan-Hernandez, N. Rodriguez-Alvarez, A. Camps, X. Bosch-Lluis, I. Ramos-Perez, and E. Valencia, "Correction of the sea state impact in the L-band brightness temperature by means of delay-Doppler maps of Global Navigation Satellite signals reflected over the sea surface," *IEEE Trans. Geosci. Remote Sens.*, vol. 46, no. 10, pp. 2914-2923, Oct. 2008.

[28] E. Valencia, A. Camps, X. Bosch-Lluis, N. Rodriguez-Alvarez, I. Ramos-Perez, F. Eugenio, and J. Marcello, "On the use of GNSS-R data to correct L-band brightness temperatures for sea-state effects: Results of the ALBATROSS field experiments," *IEEE Trans. Geosci. Remote Sens.*, vol. 49, no. 9, pp. 3225-3235, Sep. 2011.

[29] E. Valencia, A. Camps, H. Park, and N. Rodriguez-Alvarez, "Oil slicks detection using GNSS-R," in *Proc. IEEE Int. Geosci. Remote Sens. Symp.*, Vancouver, Canada, pp. 4383-4386, Jul. 2011.

[30] C. Li and W. Huang, "Sea surface oil slick detection from GNSS-R delay-Doppler maps using the spatial integration approach," in *Proc. IEEE Radar Conf.*, Ottawa, Canada, 2013.

[31] C. Li, W. Huang, and S. Gleason, "Dual antenna space-Based GNSS-R ocean

surface mapping: Oil slick and tropical cyclone sensing," *IEEE J. Sel. Topics Appl. Earth Observ. Remote Sens.*, vol. 8, no. 1, pp. 425-435, 2015.

[32] M. Martin-Neira, C. Buck, S. Gleason, M. Unwin, M. Caparrini, E. Farr'es, Olivier Germain, G. Ruffini, and F. Soulat, "Tsunami detection using the PARIS concept," in *Prog. Electromagn. Res. Symp.*, Hangzhou, China, Aug. 2005.

[33] R. Stosius, G. Beyerle, A. Hoechner, J. Wickert, and J. Lauterjung, "The impact on tsunami detection from space using GNSS-reflectometry when combining GPS with GLONASS and Galileo," *Nat. Hazards Earth Syst. Sci.*, vol. 47, no. 5, pp. 843-853, Mar. 2011.

[34] E. Valencia, A. Camps, J. F. Marchan-Hernandez, P. Hyuk, X. Bosch-Lluis, N. Rodriguez-Alvarez, and I. Ramos-Perez, "Ocean surface's scattering coefficient retrieval by delay-Doppler map inversion," *IEEE Geosci. Remote Sens. Lett.*, vol. 8, no. 4, pp. 750-754, 2011.

[35] Q. Yan and W. Huang, "GNSS-R Delay-Doppler Map simulation based on the 2004 Sumatra-Andaman tsunami event," *J. Sensors*, vol. 2016, p. ID 2750862, 2016.

[36] Q. Yan and W. Huang, "A process to simulate GNSS-R delay-Doppler map of tsunami-dominant sea surface," in *Proc. IEEE OCEANS*, Washington DC, USA, 2015.

[37] D. A Walker, "Observations of tsunami "shadows": A new technique for assessing tsunami wave heights?," *Sci. of Tsunami Hazards*, vol. 14, pp. 3-11, 1996.

[38] O. A. Godin, "Air-sea interaction and feasibility of tsunami detection in the open ocean," *J. Geophys. Res.*, vol. 109, no. 5, pp. 1-20, May. 2004.

[39] S. Gleason, V. Zavorotny and S. Lowe, "Remote sensing using bistatic GNSS reflections," in *GNSS Applications and Methods*, S. Gleason and D. Gebre-Egziabher (editors), Artech House, 2009.

[40] M. Clarizia, "Investigating the effect of ocean waves on GNSS-R microwave remote sensing measurements," PhD Thesis, University of Southampton, 2012.

[41] V. U. Zavorotny and A. G. Voronovich, "Scattering of GPS signals from the ocean with wind remote sensing application," *IEEE Trans. Geosci. Remote Sens.*, vol. 38, no. 2, pp. 951-964, 2000.

[42] C. Li, "Sea surface oil slick detection and wind field measurement using Global Navigation Satellite System Reflectometry," Master's Thesis, Memorial University of Newfoundland, 2014.

[43] C. Cox and W. Munk, "Measurement of the roughness of the sea surface from photographs of the sun's glitter," *J. Opt. Soc. Amer.*, vol. 44, pp. 838-850, Nov. 1954.

[44] S. J. Katzberg, O. Torres, and G. Ganoe, "Calibration of reflected GPS for tropical storm wind speed retrievals," *Geophys. Res. Lett.*, vol. 33, no. 18, Sep. 2006.

[45] A. Awada, A. Khenchaf, and A. Coatanhay, "Frequency impact on the bistatic

radar scattering from an ocean surface," in *Proc. IEEE Int. Geosci. Remote Sens. Symp.*, pp. 4459-4462, 2007.

[46] J. Gower, "The 26 December 2004 tsunami measured by satellite altimetry," *Int. J. Remote Sens.*, vol. 28, Nos. 13-14, pp. 2897-2913, 2007.

[47] J. F. Marchan-Hernandez, A. Camps, N. Rodriguez-Alvarez, E. Valencia, X. Bosch-Lluis, and I. Ramos-Perez, "An efficient algorithm to the simulation of Delay-Doppler maps of reflected global navigation satellite system signals," *IEEE Trans. Geosci. Remote Sens.*, vol. 47, no. 8, pp. 2733-2740, Aug. 2009.

[48] H. Park, E. Valencia, and N. Rodriguez-Alvarez, "New approach to sea surface wind retrieval from GNSS-R measurements," in *Proc. IEEE Int. Geosci. Remote Sens. Soc.*, Vancouver, Canada, pp. 1469-1472, Jul. 2011.

[49] Q. Yan and W. Huang, "Tsunami detection and parameter estimation from GNSS-R delay-Doppler map," *IEEE J. Sel. Topics Appl. Earth Observ. Remote Sens.*, to be accepted subject to minor revision.

[50] A. Helm, R. Stosius, G. Beyerle, O. Montenbruck, and M. Rothacher, "Status of GNSS reflectometry related receiver developments and feasibility studies within the German Indonesian Tsunami Early Warning System," in *Proc. IEEE Int. Geosci. Remote Sens. Symp.*, Barcelona, Spain, pp. 5084-5087, Jul. 2007.

[51] M. Van der Meijde. (2005). *Characteristics of tsunamis* [Online]. Available: http://www.itc.nl/library/Papers_2005/tsunami/Tsunami.pdf

[52] J. Tsai, B. Tsuang, P. Lu, K. Chang, M. Yap, and Y. Shen, "Measurements of

aerodynamic roughness, Bowen ratio, and atmospheric surface layer height by eddy covariance and tethersonde systems simultaneously over a heterogeneous rice paddy," *J. Hydrometeorol*, vol. 11, no. 2, pp. 452-466, Apr. 2010.

[53] C. Ruf, A. Lyons, M. Unwin, J. Dickinson, R. Rose, D. Rose, and M. Vincent, "CYGNSS: Enabling the future of hurricane prediction," *IEEE Geosci. Remote Sens. Mag.*, vol. 1, no. 2, pp. 52-67, Jun. 2013.